

A new insight into the vertical differences in NO₂ heterogeneous reaction to produce HONO over inland and marginal seas

Chengzhi Xing^a, Shiqi Xu^g, Yuhang Song^b, Cheng Liu^{b,a,c,d,*}, Yuhan Liu^f, Keding Lu^{e,*}, Wei Tan^a, Chengxin Zhang^b, Qihou Hu^a, Shanshan Wangⁱ, Hongyu Wu^h, and Hua Lin^h

^a Key Lab of Environmental Optics & Technology, Anhui Institute of Optics and Fine Mechanics, Hefei Institutes of Physical Science, Chinese Academy of Sciences, Hefei 230031, China

^b Department of Precision Machinery and Precision Instrumentation, University of Science and Technology of China, Hefei, 230026, China

^c Center for Excellence in Regional Atmospheric Environment, Institute of Urban Environment, Chinese Academy of Sciences, Xiamen, 361021, China

^d Key Laboratory of Precision Scientific Instrumentation of Anhui Higher Education Institutes, University of Science and Technology of China, Hefei, 230026, China

^e State Key Joint Laboratory of Environment Simulation and Pollution Control, College of Environmental Sciences and Engineering, Peking University, Beijing 100871, China

^f Department of nuclear safety, China Institute of Atomic Energy, Beijing, 102413, China

^g School of Earth and Space Sciences, University of Science and Technology of China, Hefei, 230026, China.

^h School of Environmental Science and Optoelectronic Technology, University of Science and Technology of China, Hefei, 230026, China

ⁱ Shanghai Key Laboratory of Atmospheric Particle Pollution and Prevention (LAP³), Department of Environmental Science and Engineering, Fudan University, Shanghai, 200433, China

*Corresponding authors: Cheng Liu (chliu81@ustc.edu.cn); Keding Lu (k.lu@pku.edu.cn)

1 ABSTRACT

2 Ship based multi-axis differential optical absorption spectroscopy (MAX-DOAS) measurements were conducted
3 along the marginal seas of China from 19 April to 16 May 2018 to measure the vertical profiles of aerosol, nitrogen
4 dioxide (NO₂), and nitrous acid (HONO). Along the cruise route, we found five hot spots with enhanced
5 tropospheric NO₂ VCDs in Yangtze River Delta, Taiwan straits, Guangzhou-Hong Kong-Macao Greater Bay areas,
6 Zhanjiang Port, and Qingdao port. Enhanced HONO concentrations could usually be observed under high-level
7 aerosol and NO₂ conditions, whereas the reverse was not always the case. To understand the impacts of relative
8 humidity (RH), temperature, and aerosol on the heterogeneous reaction of NO₂ to form HONO in different scenes, the
9 Chinese Academy of Meteorological Sciences (CAMS) and Southern University of Science and Technology (SUST)
10 MAX-DOAS stations were selected as the inland and coastal cases, respectively. The RH turning points in CAMS and
11 SUST cases were both ~65% (60–70%), whereas two turning peaks (~60% and ~85%) of RH were found in the sea
12 cases. As temperature increased, the HONO/NO₂ ratio decreased with peak values appearing at ~12.5°C in CAMS,
13 whereas the HONO/NO₂ gradually increased and reached peak values at ~31.5°C in SUST. In the sea case, when the
14 temperature exceeded 18.0°C, the HONO/NO₂ ratio rose with increasing temperature and achieved its peak at ~25.0°C.
15 This indicated that high temperature can contribute to the secondary formation of HONO in the sea atmosphere. In the
16 inland case, the correlation analysis between HONO and aerosol in the near-surface layer showed that the ground
17 surface is more crucial to the formation of HONO via the heterogeneous reaction of NO₂; however, in the coastal and
18 sea cases, the aerosol surface contributed more. Furthermore, we discovered that the conversion rate of NO₂ to HONO
19 through heterogeneous reaction in the sea case is larger than that in the inland case in higher atmospheric layers (>
20 600 m). Three typical events were selected to demonstrate three potential contributing factors of HONO production
21 under marine conditions (i.e., transport, NO₂ heterogeneous reaction, and unknown HONO source). This study
22 elucidates the sea-land and vertical differences in the forming mechanism of HONO via the NO₂ heterogeneous
23 reaction and provides deep insights into tropospheric HONO distribution, transforming process, and environmental
24 effects.
25

26 1 Introduction

27 Nitrous acid (HONO) is an important part of the atmospheric nitrogen cycle and plays a significant role in
28 atmospheric oxidation capacity (Alicke et al., 2003; Kleffmann et al., 2005). Photolysis of HONO in near ultraviolet
29 bands (Eq. 1) is a substantial source of hydroxyl radicals (OH radicals), which are one of the most important oxidants
30 in the tropospheric atmosphere. Earlier studies reported that the contribution of HONO photolysis to OH radicals can

31 reach 40–60%, while exceeding 80% in the early morning (Michoud et al., 2012; Ryan et al., 2018; Xue et al., 2020).
32 OH radicals can oxidize and destroy most atmospheric pollutants, such as CO, NO_x (NO+NO₂), SO₂, and volatile
33 organic compounds (VOCs), thereby further promoting the formation of secondary pollutants (e.g., ozone (O₃),
34 peroxyacetyl nitrate (PAN), and secondary aerosols) and leading to serious haze pollution events (Huang et al., 2014).
35 Additionally, as a nitrosating agent, HONO can produce carcinogenic nitrite amines that pose a threat to human health
36 (Zhang et al., 2015). Therefore, a full understanding of the source and formation mechanism of HONO is
37 scientifically significant for the study of tropospheric oxidation and the control of secondary pollution.

38 Currently, the known sources of HONO mainly include direct emissions from vehicles, ships, biomass burning and
39 soil, the homogeneous reaction of NO and OH radicals (Eq. 2), the nighttime and daytime heterogeneous reaction of
40 NO₂ (Eq. 3) on aerosols, vegetation, ground and other types of surfaces, and the photolysis of nitrate particles (Eq. 4)
41 (Alicke et al., 2003; Stemmer et al., 2006; Indarto et al., 2012; Wang et al., 2015; Salgado and Rossi, 2002; Zhou et
42 al., 2011). Sources of HONO exist that are poorly understood (Fu et al., 2019). The heterogeneous reaction of NO₂ as
43 a source of HONO has received continuous attention in recent years. It was found that the heterogeneous reaction of
44 NO₂ is one of the most important sources of HONO in a variety of scenes such as inland, coastal cities, and offshore
45 seas. Liu et al. (2021) reported the contribution of heterogeneous reaction of NO₂ on aerosol surface to HONO is
46 19.2% in summer, and this contribution on aerosol and ground surfaces to HONO can reach 54.6% in winter in
47 Beijing. Yang et al. (2021) and Zha et al. (2014) found that the generation rate of HONO through the heterogeneous
48 reaction of NO₂ under sea-wind conditions could elevate 3–4 times than that under land-wind conditions in the
49 northern coastal city of Qingdao and the southern coastal city of Hong Kong, respectively. Cui et al. (2019) illustrated
50 that the heterogeneous reaction of NO₂ on aerosol and sea surfaces is an important source of HONO in East China Sea
51 in summer. The process of HONO formed from the heterogeneous reaction of NO₂ is affected by various atmospheric
52 parameters. The relative humidity (RH), temperature, solar radiation intensity (SRI), and aerosol concentration and its
53 relative surface area are the particularly important parameters. Earlier works always used the linear regression
54 relationship between HONO/NO₂ and the above parameters to characterize the influence of these parameters on the
55 formation of HONO through the heterogeneous reaction of NO₂. Although this kind of simple linear regression
56 method may lead to artificial correlations and misleading conclusions, considering the vertical evolution of
57 atmospheric parameters. Wen et al. (2019) found that the increased temperature could promote the heterogeneous
58 reaction of NO₂ to form HONO in sea conditions. The generation rate of HONO could increase rapidly, when the
59 temperature was greater than 20 °C. Gil et al. (2019) found that the HONO formed from the heterogeneous reaction of
60 NO₂ will increase along with the increase of RH when RH was less than 80% in a case of land park using deep
61 learning forced by measurement results. Fu et al. (2019) reported that RH and SRI were the main parameters driving
62 the heterogeneous reaction of NO₂ to form HONO in Pearl River Delta, and it contributes to 72% of the total source
63 of HONO. Cui et al. (2019) found that the potential of heterogeneous reaction of NO₂ to form HONO will increase
64 with the increase of particle concentration and the specific surface area of single particle in coastal cities.



69 However, earlier researches generally focused on the near-surface layer of a single scene, and attentions to the
70 influence mechanism of the heterogeneous reaction of NO₂ to form HONO in vertical direction and in different sea
71 and land scenes are insufficient, which limits the comprehensive assessment to understand the sea-land differences
72 and impact mechanism of HONO formed from the heterogeneous reaction of NO₂. NO₂ could be transported from
73 inland and coastal cities to offshore seas (Tan et al., 2018). This part of NO₂ can promote the HONO formation
74 through heterogeneous reaction on the high-level aerosol and sea surfaces in the atmosphere of sea (Zhang et al.,
75 2020). The formed HONO is likely to be carried to land cities at night by sea breeze, which will affect the
76 atmospheric oxidation and air quality, and even endanger human health. Additionally, the vertical distributions and
77 values of atmospheric meteorology and aerosol parameters are significantly different in land and sea scenes, which
78 provide different conditions for the heterogeneous reaction of NO₂ to form HONO in different height layers.
79 Furthermore, aerosols and NO₂ have complex evolution and transmission characteristics in the vertical direction. The
80 vertical upward transport of aerosol and NO₂ can promote the HONO formation through heterogeneous reaction at
81 high altitude, and the vertical downward transport of HONO will impact the atmospheric environment near the ground.
82 The vertical observations in land-sea scenes are also helpful to distinguish the contribution of the heterogeneous
83 reaction of NO₂ on the aerosol and ground/sea surfaces (Zhang et al., 2020).

84 Currently, a variety of HONO measurement techniques have been developed, which in principle can be roughly
85 divided into wet chemical, spectroscopy, and mass spectrometry methods (Cheng et al., 2013; Bernard et al., 2016;
86 Gil et al., 2019; Guo et al., 2020; Jordan et al., 2020). However, these technical methods can only measure the HONO

87 information near the surface layer. Taking tower and aircraft as platforms, these techniques were performed to
88 measure HONO vertical profiles, and it was found that the peak values of HONO usually appeared under 200 m at
89 urban and suburban areas (Kleffmann et al., 2003; Stemmler et al., 2006; Zhang et al., 2009; Wong et al., 2012; Meng
90 et al., 2020; Zhang et al., 2020). These studies also revealed that the heterogeneous reaction of NO₂ on multiple
91 surfaces (ground and aerosol etc.) was an important source of HONO under planetary boundary layer (PBL),
92 especially in haze days. Furthermore, they also reported that the HONO/NO₂ ratios usually decreased with the
93 increase of height under 200 m at inland and coastal areas. However, the cost of above techniques used to measure
94 HONO vertical profiles was too high, and the real-time and continuous measurement cannot be realized. Multi-axis
95 differential optical absorption spectroscopy (MAX-DOAS), as a ground-based ultra-hyperspectral remote sensing
96 technology, was widely used for vertical observation of atmospheric pollutants in the past two decades. In the past
97 five years, several researchers carried out campaigns based on MAX-DOAS to measure the vertical profile of HONO
98 in inland and coastal areas, and revealed their vertical characteristics, sources, and the contribution to atmospheric
99 oxidation at different height layers (Garcia-Nieto et al., 2018; Ryan et al., 2018; Wang et al., 2020; Xing et al., 2021;
100 Xu et al., 2021; He et al., 2023). Few studies were conducted on the sources of HONO at different height layers in sea
101 conditions. In this study, MAX-DOAS is used for the first time to study the spatiotemporal distribution and the
102 sources of HONO along the Chinese coastline, and to learn the differences of the HONO formed from the
103 heterogeneous reaction of NO₂ in different height layers and land-sea scenes.

104 **2 Methods and methodologies**

105 **2.1 Measurement cruise**

106 The ship-based atmospheric observation campaign along the marginal seas of China was conducted from 19 April to
107 16 May 2018. The latitude and longitude ranges of the entire campaign covered 21.12°N–35.89°N and
108 110.67°E–122.16°E. The detailed voyage records of the observation ship are shown in Table 1. An integrated and
109 fully automated MAX-DOAS instrument was installed aboard the stern deck of the ship (Figure S1(a)). To ensure that
110 the instrument is always kept in a horizontal position, a photoelectric gyro was used. The angle between the
111 observation and heading directions of the ship was always maintained at 135° during the whole campaign. The
112 telescope unit of the instrument pointed towards sea during cruise NO.3 and NO.6. The telescope unit pointed towards
113 inland during cruise NO.1, NO.4, and NO.5. During cruise NO.2, the observation telescope always pointed to
114 Chongming island. The measurement ship only sailed in daytime from 19 April to 02 May, and continuously sailed in
115 all the daytime and nighttime from 3 May to 16 May 2018. The ship docked in Daishan port on 9–10 May and no
116 observations were conducted during these two days.

117 The aim of this campaign was to learn the vertical differences of NO₂ heterogeneous reaction to produce HONO in
118 marginal seas of China and compare the influence mechanism of that in inland cities. To fully understand the
119 differences of the impacts of RH, temperature, and aerosol on the HONO secondary formation in land and sea
120 conditions, the Chinese Academy of Meteorological Sciences (CAMS) and Southern University of Science and
121 Technology (SUST) MAX-DOAS stations were selected as inland and coastal areas for analysis, respectively. CAMS
122 is located in the urban of Beijing (116.32°E, 39.94°N), and SUST is located in Shenzhen (114.00°E, 22.60°N) (Figure
123 S2). This study will provide scientific guidance for understanding regional oxidation capacity and controlling the
124 secondary air pollution.

125 **2.2 MAX-DOAS measurements**

126 **2.2.1 Instrument setup**

127 The compact instrument consists of an ultraviolet spectrometer (AvaSpec-ULS2048L-USB2, 300–460 nm spectral
128 range, 0.6 nm spectral resolution) at a 20°C fixed temperature with a deviation of < 0.01°C, a one-dimensional CCD
129 detector (Sony ILX511, 2048 individual pixels) and a telescope unit driven by a stepper motor to collect scattered
130 sunlight from different elevation angles. The accuracy of elevation angle is < 0.1° and the telescope field of view
131 (open angle) is < 0.3°. A full scanning sequence consists of 11 elevation angles (1°, 2°, 3°, 4°, 5°, 6°, 8°, 10°, 15°, 30°,
132 and 90°). The integration time of one individual spectrum was set to 30 s, and each scanning sequence took about 5.5
133 min. Besides, the controlling electronic devices and connecting fiber are mounted inside. The instrument is equipped
134 with a high-precision Global Position System (GPS) to record the real-time coordinated positions of the cruise ship.
135 The detailed description of the setup of MAX-DOAS in CAMS and SUST can be found in Liu et al. (2021).

136 **2.2.2 Data processing and filtering**

137 The MAX-DOAS measurements could be influenced by the exhaust from the measurement ship. Therefore, the data
138 contaminated by the exhaust were filtered out. As shown in Figure S1(b), the direction and speed of the plume
139 exhausted from the ship depends on the ship and the true wind speeds/directions. Individual measurements taken
140 under unfavorable plume directions (plume directions between 45 and 135° with respect to the heading of the ship)
141 were discarded. To avoid the strong influence of the stratospheric absorption, the spectra measured with solar zenith
142 angle (SZA) larger than 75° were filtered out. Under these two filtering criteria, 4.9 and 8.3% of all data were rejected
143 before DOAS analysis (Xing et al., 2017, 2019, 2020).

144 2.2.3 DOAS analysis

145 The MAX-DOAS measured spectra were analyzed using the software QDOAS which is developed by BIRA-IASB
146 (<http://uv-vis.aeronomie.be/software/QDOAS/>). The DOAS fit results are the differential slant column densities
147 (DSCDs), i.e. the difference of the slant column density (SCD) between the off-zenith and the corresponding zenith
148 reference spectra. Details of the DOAS fit settings are listed in Table 1. A typical DOAS retrieval example for the
149 oxygen dimer (O₄), nitrogen dioxide (NO₂), and nitrous acid (HONO) are shown in Figure 1. The stratospheric
150 contribution was approximately eliminated by taking the zenith spectra of each scan as reference in the DOAS
151 analysis. Before profile retrieval, DOAS fit results of O₄, NO₂, and HONO with root mean square (RMS) of residuals
152 larger than 3×10^{-3} were filtered. Furthermore, the SCD data under the color index (CI) being $< 10\%$ of the thresholds
153 obtained through fitting a fifth-order polynomial to CI data which is a function of time was filtered out to ensure a
154 high signal-to-noise ratio (SNR) of the spectra. This filtering criteria remove 2.1, 3.9, and 5.3% for O₄, NO₂, and
155 HONO, respectively.

156 2.3 Vertical profile retrieval

157 Aerosol and trace gases (i.e., NO₂ and HONO) vertical profiles are retrieved from MAX-DOAS measurements using
158 the algorithm reported by Liu et al. (2021). The inversion algorithm is developed based on the Optical Estimation
159 Method (OEM) (Rodgers, 2000), which employs the radiative transfer model VLIDORT as the forward model. The
160 detailed retrieval procedure is displayed in Appendix I and Figure S3.

161 In this study, an exponential decreasing a priori with a scale height of 1.0 km was used as the initial profile for both
162 the aerosol and trace gases retrieval (Figure S4). The surface concentrations of aerosol, NO₂, and HONO were set to
163 0.2 km^{-1} , 3.0 ppb, and 1.0 ppb, respectively. We assume a fix set of aerosol optical properties with asymmetry
164 parameter of 0.69, a single scattering albedo of 0.90, and ground albedo of 0.05. Furthermore, the uncertainty of the
165 aerosol and trace gases a priori profile was set to 100% and the correlation length was set to 0.5 km. The averaging
166 kernels indicated that the sensitivity of the profile retrieval tended to decrease with increasing altitude, and was
167 especially sensitive to the layers within 0–1.5 km (Figure S5). The sum of the diagonal elements in the averaging
168 kernel matrix is the degrees of freedom (DOF), which denotes the number of independent pieces of information
169 contained in the measurements.

170 2.4 Error analysis

171 For profile retrieval, the error sources can be divided into four different types: smoothing error, measurement noise
172 error, forward model error, and model parameter error (Rodgers, 2004). However, in terms of this classification, some
173 errors are difficult to be calculated or estimated. For example, forward model error, which is caused by an imperfect
174 representation of the physics of the system, is hard to be quantified due to the difficulty of acquiring an improved
175 forward model. Given calculation convenience and contributing ratios of different errors in total error budget, we
176 mainly took into account error sources based on the following classification, which were smoothing and noise errors,
177 algorithm error, cross section error, and uncertainty related to the aerosol retrieval (only for trace gas). Here, we
178 estimated the contribution of different error sources to the trace gas vertical column densities (VCDs) and AOD, and
179 near-surface (0–200 m) trace gas concentrations and aerosol extinction coefficients (AECs), respectively. The detailed
180 demonstrations and estimation methods are displayed below, and the final results are summarized in Table 3.

- 181 a. Smoothing errors arise from the limited vertical resolution of profile retrieval. Measurement noise errors denote
182 the noise in the spectra (i.e., the fitting error of DOAS fits). They can be quantified by averaging the error of
183 retrieved profiles, as the error of the retrieved state vector equals the sum of these two independent errors. We
184 calculated the sum of smoothing and noise errors on near-surface concentrations and column densities, which
185 were 14 and 5 % for aerosols, 16 and 17 % for NO₂, and 20 and 22 % for HONO, respectively in the sea scene.
186 The corresponding values were 13 and 5 % for aerosols, 14 and 16 % for NO₂, and 18 and 20 % for HONO,
187 respectively at SUST and 13 and 5 % for aerosols, 15 and 17 % for NO₂, and 19 and 21 % for HONO at CAMS.
- 188 b. Algorithm error is the discrepancy between the measured and modelled DSCDs. This error contains forward
189 model error from an imperfect approximation of forward function (e.g., spatial inhomogeneities of absorbers and
190 aerosols), forward model parameter error from selection of parameters, and error not related to the forward
191 function parameters, such as detector noise (Rodgers, 2004). Algorithm error is a function of the viewing angle,
192 and it is difficult to assign this error to each altitude of profile. Usually, the algorithm errors on the near-surface
193 values and column densities are estimated by calculating the average relative differences between the measured
194 and modeled DSCDs at the minimum and maximum elevation angle (except 90 °), respectively (Wagner et al.,
195 2004). Considering its trivial role in the total error budget, we estimated these errors on the near-surface values
196 and the column densities at 4 and 8 % for aerosols, 3 and 11 % for NO₂, and 20 and 20 % for HONO, according
197 to Wang et al. (2017) and Wang et al. (2020).
- 198 c. Cross section error is the error arising from an uncertainty in the cross section. According to Thalman and
199 Volkamer, (2013), Vandaele et al. (1998), and Stutz et al. (2000), we adopted 4, 3, and 5 % for O₄ (aerosols), NO₂,
200 and HONO, respectively.
- 201 d. The trace gas profile retrieval error represents the one, which is sourced from aerosol extinction profile retrieval
202 and propagated to retrieved trace gas profile. This error could be roughly estimated based on a linear propagation
203 of the total error budgets of the aerosol retrievals. The errors of trace gases were roughly estimated at 15% for

VCDs and 10% for near-surface concentrations for the two trace gases in the sea scene. The corresponding values were 14 and 10 % for near-surface concentrations and VCDs, respectively at SUST, and 14 and 10 % at CAMS. The total uncertainty was calculated by adding all the error terms in the Gaussian error propagation, and the final results were listed in the bottom row of Table 3. We found that the sum of smoothing and noise errors played a dominant role in the total uncertainty.

2.5 Ancillary data

Meteorological data (including temperature, pressure, relative humidity, visibility, solar radiation intensity, wind speed, and wind direction) with a temporal resolution of 1 min was measured in the weather station installed on the ship. NO was measured using NO analyzer (Thermo Scientific model 42i) with a 1 min resolution. The speed of the ship was calculated referring to the GPS data.

The temperature and relative humidity of two ground-based stations (i.e., CAMS and SUST) were collected from Weather Underground website, temporal resolution of which is around 3 hours.

The backward trajectory was calculated using HYSPLIT (Hybrid Single-Particle Lagrangian Integrated Trajectory) developed by the National Oceanic and Atmospheric Administration Air Resource Laboratory (NOAA-ARL). The meteorological data with a $1^{\circ}\times 1^{\circ}$ spatial resolution and 24 layers were collected from the Global Data Assimilation System (GDAS).

3 Results and Discussion

3.1 Overview of the MAX-DOAS observation over marginal seas of China

A radiative transfer model SCIATRAN was used to convert SCDs of NO_2 and HONO to their tropospheric VCDs. The vertical profiles of aerosol, NO_2 , and HONO retrieved from MAX-DOAS, the temperature and pressure vertical profiles simulated using a dynamical-chemical model (WRF-Chem), and the geo-position data collected by GPS were introduced as inputs in SCIATRAN for the NO_2 and HONO air mass factor (AMF) calculation. Missing data are due to power and instrument system failure, interference of ship plume, unfavorable weather condition (i. e., heavy rain), and night sailing. During the cruise of Chongming to Zhanjiang, NO_2 VCDs varied from 1.05×10^{14} to 4.02×10^{16} molec. cm^{-2} with an averaged value of 3.90×10^{15} molec. cm^{-2} . From Zhanjiang to Qingdao, NO_2 VCDs varied from 1.08×10^{14} to 2.60×10^{16} molec. cm^{-2} with an averaged value of 4.27×10^{15} molec. cm^{-2} . From Chongming to Zhanjiang, HONO VCDs varied from 1.00×10^{14} to 2.58×10^{15} molec. cm^{-2} with a mean value of 2.39×10^{14} molec. cm^{-2} . From Zhanjiang to Qingdao, HONO VCDs varied from 1.01×10^{14} to 2.61×10^{15} molec. cm^{-2} with a mean value of 2.74×10^{14} molec. cm^{-2} .

Figure 2 showed the spatial distribution of NO_2 and HONO VCDs over the marginal seas of China. Five enhanced tropospheric NO_2 VCDs hot spots were observed during the whole campaign, i.e., the coastal areas of Yangtze River Delta, Taiwan straits, Guangzhou-Hong Kong-Macao Greater Bay areas, Zhanjiang Port, and Qingdao port. In the coastal areas of Yangtze River Delta, the hot spots were mainly distributed in the Yangtze River estuary, Hangzhou Bay, Ningbo port, Taizhou port, and Wenzhou port. These areas are mostly important shipping channels or shipping ports, and are great NO_2 emission sources. The averaged NO_2 VCDs in above five areas reached 1.07×10^{16} , 1.30×10^{16} , 7.27×10^{15} , 5.34×10^{15} , and 3.12×10^{15} molec. cm^{-2} , respectively (Figure S6(a)). HONO exhibited similar spatial distribution characteristics as NO_2 , and the averaged HONO VCDs in above five hot-spot areas reached 1.01×10^{15} , 7.91×10^{14} , 6.02×10^{14} , 5.36×10^{14} , and 5.17×10^{14} molec. cm^{-2} , respectively (Figure S6(b)). It indicates that NO_2 is an important precursor of HONO. Earlier studies reported that HONO can be generated from NO_2 through heterogeneous reaction on the surface of aerosol and sea (Yang et al., 2021). However, there are obvious differences in the concentration distribution of HONO and NO_2 in the southeast coastal area of Jiangsu (from Qidong to Dongtai). In this area, NO_2 showed a higher concentration (1.66×10^{16} molec. cm^{-2} , which is 4 times higher than the mean NO_2 VCD), while HONO showed a lower concentration (2.06×10^{14} molec. cm^{-2} , which is ~80% of the mean HONO VCD). It may be the fresh ship emission plume on the route enhancing the NO_2 concentration and HONO has not been fully formed from NO_2 heterogeneous reaction in time, since the observations from ship-based MAX-DOAS are instantaneous.

The surface concentration of NO_2 and HONO were extracted from their corresponding vertical profiles. As shown in Figure 3, the total averaged near-surface NO_2 concentrations under sea-oriented and land-oriented measurements were 8.46 and 11.31 ppb, respectively. The total averaged near-surface HONO concentrations were 0.23 and 0.27 ppb under sea-oriented and land-oriented measurements. The total averaged near-surface HONO/ NO_2 ratios in sea-oriented and land-oriented measurements were 0.027 and 0.024, respectively. Earlier studies reported that vehicle and ship emissions were the main primary HONO sources on land and sea, respectively, and NO_2 heterogeneous reaction on the surfaces of ground, sea, vegetation, and aerosol were the important secondary HONO sources (Liu et al., 2021). Additionally, they found that the surface HONO concentration under the sea case was lower than that under the land case, especially in the morning and evening (Yang et al., 2021). Figure 4 showed the time series of AOD, the surface concentrations of NO_2 and HONO, and the surface HONO/ NO_2 during the whole campaign. We found that the time series of AOD and NO_2 were similar. The high AOD and NO_2 usually appeared in busy shipping channels and ports, and the obvious high-value areas were the coast of the Yangtze River Delta, the Taiwan Strait, Xiamen port, Zhanjiang port, and Qingdao port (with mean AOD and NO_2 of 1.28 and 18.90 ppb, respectively). HONO always

263 appeared under high AOD and NO₂ conditions, however, high AOD and NO₂ were not necessarily accompanied with
264 high HONO concentration. This was because the heterogeneous formation of HONO requires suitable meteorological
265 conditions (i.e., RH and temperature) in addition to its precursor (NO₂) and the reaction surface (aerosol) (Liu et al.,
266 2019). The high HONO/NO₂ values were found on 02, 13, and 14 May with an average value of 0.45. Furthermore,
267 we found the high values of HONO/NO₂ always appeared from 11:00 to 14:00 during a whole day.

268 **3.2 Relationship between HONO/NO₂ with RH, Temperature, and aerosol in land and sea**

269 Sun et al. (2020) reported that HONO concentrations could increase up to 40–100% over the shipping routes and
270 international ports, and Huang et al. (2017) reported vehicle exhaust could contribute to ~12–49% of the atmospheric
271 HONO budget. Since the direct emissions of the measurement ship were removed before data analysis, the primary
272 source of HONO during the whole campaign was mainly from the direct emissions of cargo ships. By subtracting the
273 average marine background of NO_x and HONO from the ship plume emission values, the impact of background
274 values is reduced and the emission ratio of $\Delta\text{HONO}/\Delta\text{NO}_x$ can be obtained, and this emission ratio can be used for
275 quantifying the primary HONO (Sun et al., 2020; Xu et al., 2015). In this study, we used an averaged $0.46 \pm 0.31\%$
276 emission ratio of $\Delta\text{HONO}/\Delta\text{NO}_x$ referring to Sun et al. (2020) to understand the primary source of HONO on the sea
277 surface during the campaign. The NO was measured using in situ instrument, and sea-surface NO₂ was extracted from
278 the retrieved NO₂ vertical profiles (NO_x = NO + NO₂). Additionally, the calculation method of emission ratios of
279 $\Delta\text{HONO}/\Delta\text{NO}_x$ in CAMS and SUST was referred from Xu et al. (2015), Liu et al. (2018), and Xing et al. (2021)
280 (Appendix II). The averaged emission ratios in CAMS and SUST were $0.82 \pm 0.34\%$ and $0.79 \pm 0.31\%$, respectively.
281 The direct emissions were deduced in the following study of the secondary formation of HONO. The ratios of
282 HONO/NO₂ in CAMS, SUST, and the ship-based campaign could be found in Figure S7. Furthermore, the main
283 secondary formation pathway of HONO is considered as the heterogeneous reaction of NO₂ on the surface. The linear
284 regression between HONO and NO₂ in land and static sea scenarios is shown in Figure 5. We found the fitting slopes
285 in static sea scenes was ~8–10 times larger than that in land scenes, especially on sea-oriented measurements under
286 static weather condition (slope ≈ 0.06). The correlation coefficients (R) in inland and static sea scenarios were all >
287 0.62, except in SUST (R = 0.58), which indicates the formation rate of secondary HONO from NO₂ heterogeneous
288 reaction in static sea scenarios may be faster than that in land scenarios. The corresponding temperature and RH
289 conditions of each spot are displayed in Figure S8, which roughly reveals the impact of RH and temperature on the
290 process of NO₂ forming HONO through heterogeneous reactions.

291 **3.2.1 RH dependence on HONO formation**

292 The scatter plots of HONO/NO₂ against RH in different land and sea conditions are illustrated in Figure 6. The
293 highest values can represent varying range of data in each interval and reveal concentration levels of data distribution.
294 To eliminate the influence of other factors, the average of the six highest HONO/NO₂ in each 10% RH interval is
295 calculated to reflect the distribution range of data in each interval (Liu et al., 2019). The dependence of the averaged
296 top-6 HONO/NO₂ on RH reveal an overall variation tendency of HONO/NO₂ against RH. In the inland (CAMS) and
297 coastal (SUST) cases, the RH turning points are both ~65% (60–70%), where increasing trend switches to decreasing
298 tendency. The HONO/NO₂ increases along with RH when RH is less than 65%, and the HONO/NO₂ will decrease
299 when RH is larger than 65%, which implies that it contributes to the HONO formation from the heterogeneous
300 reaction of NO₂ on wet surfaces with the gradual increase of RH until 65%. The decrease of HONO/NO₂ with RH
301 larger than 65% is presumably due to the efficient uptake of HONO on wet surfaces, and the wet surfaces being less
302 accessible or less reactive to NO₂ when RH being larger than 65% (Liu et al., 2019). However, two turning peaks of
303 RH were found in the sea cases. The first RH turning peak occurred in ~60%, which is the similar to that under the
304 inland and coastal cases, and another RH turning peak appeared in ~85% (80–90%). This implies that high RH also
305 could increase the HONO formation in sea cases. Additionally, the HONO/NO₂ decreased sharply when RH was
306 larger than 95%, because the reaction surface will asymptotically approach a water droplet state to limit the formation
307 of HONO with RH larger than 95%.

308 **3.2.2 Temperature dependence on HONO formation**

309 The scatter plots of HONO/NO₂ against temperature in different land and sea conditions are shown in Figure 7.
310 Similar to the scatter plots of HONO/NO₂ against RH, we also adopted the averaged top-6 HONO/NO₂ values in each
311 5°C interval to represent a general variation tendency of HONO/NO₂ against temperature. In the inland condition
312 (CAMS), the HONO/NO₂ decreased along with the increase of temperature, and the highest values of HONO/NO₂
313 appeared at ~12.5°C. However, we found that HONO/NO₂ increased along with the increase in temperature, and the
314 highest values of HONO/NO₂ appeared at ~31.5°C in coastal condition (SUST), which indicates that the HONO
315 formation from NO₂ heterogeneous reaction will be accelerated under lower and higher temperature in the inland and
316 coastal conditions, respectively. In the sea condition, the HONO/NO₂ increased along with the increase in temperature
317 with a high value under ~25.0°C when the atmospheric temperature was larger than 18.0°C, and simultaneously, a
318 ~1.9 averaged HONO/NO₂ high value was found under ~15.0°C (14.0–17.0°C). Furthermore, we found that the
319 appearance of HONO/NO₂ high values under lower temperature (14.0–17.0°C) was usually accompanied by land

320 breeze. Wen et al. (2019) also reported that relatively high temperature could contribute to the formation of HONO in
321 the sea condition.

322 3.2.3 Impact of aerosol on HONO formation

323 To further understand the HONO formation from NO₂ heterogeneous reaction on aerosol surface, several correlation
324 analyses were conducted. As shown in Figure 8, the linear regression plot between HONO and aerosol in land and sea
325 conditions was performed. It was found that the correlation coefficient (R) between HONO and aerosol varied in the
326 order of coastal (0.55) > sea (0.51) > inland (0.14). Additionally, the fitting slopes under coastal and sea conditions
327 (0.07) are about 2.3 times larger than that under inland condition (0.03), which implies that the ground surface maybe
328 more important than aerosol surface during the process of HONO formed from NO₂ heterogeneous reaction in the
329 ground surface layer of the inland. In the coastal and sea conditions, the aerosol and sea are both important in
330 providing heterogeneous reaction surface for NO₂ to form HONO (Cui et al., 2019; Wen et al., 2019; Yang et al.,
331 2021). Additionally, we found the averaged values of HONO/NO₂ were 0.011±0.004, 0.014±0.006, 0.008±0.003, and
332 0.007±0.003 when aerosol extinctions are 0–0.3, 0.3–0.6, 0.6–0.9 and > 0.9 km⁻¹ in the inland case, respectively
333 (Figure 8(b)). As shown in Figure 8, the high values of HONO/NO₂ were mainly under aerosol extinction being less
334 than 1.0 km⁻¹ with averaged values of 0.012±0.006 and 0.090±0.004 in the coastal and sea cases, respectively. It
335 indicates that aerosol surface plays a more important role in forming HONO through NO₂ heterogeneous reaction in
336 the sea condition than that in the land condition.

337 3.3 Vertical distributions of HONO/NO₂ under different aerosol condition in land and sea

338 To further investigate the height dependence of HONO/NO₂ under land and sea conditions, two cases in Pearl River
339 Delta (PRD) were selected from the whole campaign. As shown in Figure 9, “A” and “B” were under similar aerosol
340 level (the extinction coefficients in surface layer being 0.45–0.60 km⁻¹) and vertical distribution structure, and were all
341 observed from 10:00 to 11:00 hrs. The instrument viewed sea accompanied with sea wind in “A” named sea scene,
342 and the instrument viewed land accompanied with land wind in “B” named land scene. The NO₂ in the sea and land
343 scenes have a similar vertical structure, and the NO₂ concentration in land scene are larger than that in sea scene
344 except on the surface layer. The HONO have the same vertical distribution structure in the above two scenes, and the
345 HONO concentration in the land scene is always larger than that in the sea scene. In Figure 9(e), we found that
346 HONO/NO₂ under 0–400 m in the land scene is higher than that in the sea scene, however, the HONO/NO₂ values are
347 obviously lower in the land scene than that in the sea scene above 400 m. Furthermore, the growth rate of HONO/NO₂
348 with the increase of height in the sea scene is significantly faster than that in the land scene above 400 m. This
349 indicates the generation rates of HONO sourced from NO₂ heterogeneous reaction on aerosol surface in the sea scene
350 is larger than that in the land scene above 400 m. Under 400 m, the HONO generation rates in the land scene is larger
351 than that in the sea scene.

352 Additionally, we selected inland cases (CAMS) to learn the difference of height dependence of HONO/NO₂ compared
353 with sea scenes under different aerosol loads. As shown in Figure 10, the sea and inland scenes had similar aerosol
354 levels (low aerosol level: < 0.2 km⁻¹) and vertical structure. Furthermore, the NO₂ and HONO in the sea and inland
355 scenes have similar vertical structure, although their concentrations in the sea scene are all larger than that in the
356 inland scene. In Figure 10(d), we found that the HONO/NO₂ in the sea scene was obviously larger than that in the
357 inland scene above 400 m. The HONO/NO₂ in the sea scene was about 4.5 times larger than that in the inland scene
358 especially above 600 m. As shown in Figure 11, the aerosols under the sea and inland scenes exhibited similar
359 extinction levels (relatively high level: ~0.8 km⁻¹) and vertical structure. The NO₂ concentration in the sea scene was
360 higher than that in the inland scene but with a similar vertical structure. The HONO concentration in the sea scene was
361 lower than that in the inland scene under 400 m, while the concentration in the sea scene was larger than that in the
362 inland scene above 400 m. In Figure 11 (d), we found the HONO/NO₂ in the inland scene was larger than that in the
363 sea scene under 600 m, while the HONO/NO₂ in the sea scene was about 2 times larger than that in the inland scene
364 above 600 m. All the above cases indicated that the HONO generation rate from NO₂ heterogeneous reaction in the
365 sea scene was larger than that in the inland scene in higher atmospheric layers above 400–600 m. The high-altitude (>
366 400–600 m) atmospheric parameters in the sea scene were more conducive to promote the HONO formation through
367 the heterogeneous reaction of NO₂. As shown in Figure S9, the ratio of HONO/NO₂ also generally increased with the
368 increase in height above 0.2 km during the whole ship-based campaign. The greatest sensitivity under 1.5 km and the
369 high degree of freedom (DOF) for aerosol, NO₂, and HONO gave confidence in the retrieval results (Figure S10).

370 3.4 Case study

371 The important factors and precursors to drive the formation of HONO through heterogeneous reaction had complex
372 evolution and transport characteristics. To further clarify the role of these parameters in the heterogeneous process of
373 NO₂ to form HONO, three typical processes were selected to reveal the favorable conditions for HONO formation at
374 the sea scene.

375 3.4.1 20 April: A typical transport event

376 As shown in Figure 12, the aerosol mainly distributed in 0–200 m with a mean extinction coefficient larger than 0.74
377 km^{-1} . NO_2 was mainly distributed near the ground surface with a mean concentration of 28.54 ppb before 13:20. The
378 NO_2 during this period may come from local ship emissions, as this area is a main shipping channel. From 14:25 to
379 17:10, a high-concentration NO_2 air mass (averaged 13.29 ppb) was found at ~ 2.0 km. To understand the source of
380 this high-altitude NO_2 air mass, we further investigated the possible influence of transport by using the backward
381 trajectories. We calculated 24 h backward trajectories of air masses at 500, 1000, and 2000 m using HYSPLIT (Figure
382 S11). In Figure S11, we found that the dominant wind direction during this period was southeast at all heights, i.e.,
383 500, 1000, and 2000 m. The transport of air masses carried NO_2 emitted by ships in Ningbo and Zhoushan ports to
384 main cargo ports of China and Shanghai. Furthermore, the concentration of NO_2 was low (averaged 2.32 ppb) near the
385 ground surface from 14:25 to 17:10. As shown in Figure 12 (e) and (g), a low pressure (< 1020 hPa), north dominant
386 wind direction with the wind speed > 12 m/s appeared at the ground surface during this period, which implies that the
387 clean air from north reduced the local surface NO_2 . The HONO was mainly distributed near the surface with a mean
388 concentration of 0.07 ppb, and the two peaks were found in the early morning (averaged 0.15 ppb) and at 12:15
389 (averaged 0.11 ppb), respectively (Figure S12). The relatively high concentration of HONO appearing in the early
390 morning was possibly attributed to the accumulation with the stabilization of boundary layer and attenuation of solar
391 radiation after sunset the day before (Xing et al., 2021). The HONO peak appearing at 12:15 may be sourced from the
392 heterogeneous reaction of NO_2 on the aerosol surface under a $\sim 80\%$ RH, 18.5°C temperature, and 1×10^3 W/m^2 SRI
393 conditions.

394 **3.4.2 28 April: A typical event of HONO produced from NO_2 heterogeneous reaction**

395 From a typical port observation case, the measurement ship moored at Xiamen port on 28 April. As shown in Figure
396 13, we found two peaks for aerosol and NO_2 from 09:00–11:00 and 14:00–16:00, respectively (averaged aerosol
397 extinction coefficient > 0.8 km^{-1} , averaged NO_2 concentration > 12.0 ppb). NO_2 was mainly distributed near the sea
398 surface layer 0–200 m, and a high-concentration NO_2 air mass was found from 1.0–2.0 km during 13:00–14:00 due to
399 the short distance transport of NO_2 emitted from ships in Xiamen port (Figure S13). However, aerosol appeared in the
400 range of 0.0–2.0 km during 09:00–11:00 and 14:00–16:00. In Figure 13 (g), we found that the wind speeds in the
401 above two peak periods were obviously higher than that in other periods. From 09:00–11:00, the wind speed was ~ 5.0
402 m/s with a northwest dominant direction (urban), and the wind speed was ~ 6.0 m/s with a southeast dominant
403 direction (port gateway) during 14:00–16:00, which indicates that the short-distance high-altitude transport caused the
404 appearance of high-extinction aerosol mass during the above two periods.

405 Furthermore, we found the high-concentration HONO only appeared at 14:00–16:00 with a 0.57 ppb averaged
406 concentration under 0.9 km, while it was only about 0.14 ppb during 09:00–11:00 period. The slight increase of RH
407 and temperature (Tem) at 14:00–16:00 (RH: $\sim 75.0\%$, Tem: 23.7°C) may contribute to HONO formation through
408 heterogeneous reaction of NO_2 on the aerosol surface than that at 09:00–11:00 (Figure 13 (d)-(e), Section 3.2).
409 Contrarily, the solar radiation intensity (SRI) (~ 600 W/m^2) at 09:00–11:00 was obviously larger than that (~ 250 W/m^2)
410 at 14:00–16:00 (Figure 13 (f)). The higher SRI accelerated the photolysis of HONO during 09:00–11:00 period (Kraus
411 et al., 1998). Therefore, the lower formation rate and higher photolysis rate lead to a significantly lower HONO
412 concentration at 09:00–11:00 than that at 14:00–16:00.

413

414 **3.4.3 03 May: A typical event with unknown HONO source**

415 The measurement ship conducted observation in the sea area near Zhanjiang on 03 May, 2018. As shown in Figure 14,
416 we found that there was an obvious sinking process for aerosol from ~ 1.0 km during 09:00–16:00, and eventually
417 accumulated near the sea surface with a high extinction coefficient > 0.92 km^{-1} . The NO_2 was mainly concentrated
418 near the sea surface layer (0–400 m) with an averaged concentration of 8.93 ppb from 08:00 to 09:00. Thereafter, with
419 the rise the planetary boundary layer (PBL) height after sunrise, NO_2 was gradually mixed and spread throughout the
420 PBL from 09:00–13:00. During this period, it was accompanied by the increase of the NO_2 concentration (averaged
421 11.2 ppb) under PBL (Figure S14). It is due to the contribution of ship emissions near the sea surface. Contrarily, the
422 regional transport of NO_2 from land also increased the NO_2 concentration in this area of the sea, with wind speed
423 increasing from 2.5 to 7.8 m/s with a north wind direction from 10:00 to 16:00 (Figure 14 (g)).

424 Several HONO peaks (> 0.2 ppb) at 0.5–1.0 km were found from 09:45 to 13:00, and the aerosol and NO_2 high values
425 were also observed at this height layer, simultaneously, which implies that the heterogeneous reaction of NO_2 on
426 aerosol surface is more important than that on the sea surface for HONO source under sea atmosphere. Additionally,
427 HONO concentration obviously elevated after 14:00, especially during 14:00–16:00 (> 0.4 ppb). It may be sourced
428 from heterogeneous reaction of NO_2 on the aerosol surface, under RH a being $\sim 92.5\%$ (Figure 14 (d)). The photolysis
429 of HONO also decreased with $\text{SRI} < 150$ W/m^2 (Figure 14 (f)) during this period. Furthermore, a HONO peak (> 0.32
430 ppb) was observed during 16:40–17:10. However, the NO_2 concentration always kept low (< 1.5 ppb) after 16:00, and
431 the temperature was lower than 17°C (Figure 14 (e)), which indicates the heterogeneous reaction of NO_2 not being
432 the source of the observed HONO peak. The wind was north dominant with an average speed at 7.8 m/s after 15:00,

433 which implies that the regional transport may not be the source of the observed high-concentration of HONO.
434 Furthermore, the SRI was lower than 87.5 W/m^2 , and it shows the photolysis of nitrate aerosol also not being the
435 source of the elevated HONO. The unknown HONO source in this area of the sea need to be further explored.

436 **4 Summary and Conclusions**

437 Currently, many uncertainties in the study of the HONO forming mechanism through the heterogeneous reaction of
438 NO_2 exist. Earlier studies mostly focused on the near-surface layer, and the assessment of the contribution of NO_2
439 heterogeneous reaction to HONO formation in the vertical direction of the boundary layer is insufficient. Therefore,
440 we aim to learn the sea-land and vertical differences of the HONO forming mechanism from NO_2 heterogeneous
441 reaction and provide deep insights into the distribution characteristics, transforming process, and environmental
442 effects of tropospheric HONO. Ship based MAX-DOAS observations along the marginal seas of China were
443 performed from 19 April to 16 May 2018. Simultaneously, two ground-based MAX-DOAS observations were
444 conducted in the inland station CAMS and the coastal station SUST to measure the aerosol, NO_2 , and HONO vertical
445 profiles.

446 Along the cruise route, we found five hot spots with enhanced tropospheric NO_2 VCDs in Yangtze River Delta,
447 Taiwan straits, Guangzhou-Hong Kong-Macao Greater Bay areas, Zhanjiang Port, and Qingdao port. Under
448 high-level NO_2 conditions in the above five hot spots, we also observed enhanced HONO levels. Contrastingly, the
449 low-concentration HONO accompanied high-level NO_2 in the southeast coastline of Jiangsu province. When peak
450 AOD and NO_2 conditions were observed, enhanced HONO were observed, although the reverse was not always the
451 case.

452 To understand the impacts of RH, temperature, and aerosol on the heterogeneous reaction of NO_2 to produce HONO,
453 the emission ratios of $\Delta\text{HONO}/\Delta\text{NO}_x$ were calculated to quantify the contribution of the primary HONO source to
454 the total production of HONO. We found that the RH turning points in CAMS and SUST cases were both $\sim 65\%$
455 ($60\text{--}70\%$), whereas two turning peaks ($\sim 60\%$ and $\sim 85\%$) of RH were found in the sea cases. This implied that high
456 RH could contribute to the secondary formation of HONO in sea atmosphere. With increase in temperature, the
457 HONO/NO_2 decreased with peak values appearing at $\sim 12.5^\circ\text{C}$ in CAMS, whereas the HONO/NO_2 gradually increased
458 and reached peak values at $\sim 31.5^\circ\text{C}$ in SUST. In the sea case, when the temperature exceeded 18.0°C , the HONO/NO_2
459 increased with the increasing temperature and achieved peak at $\sim 25.0^\circ\text{C}$. This indicated that high temperature could
460 promote the secondary formation of HONO in the sea and coastal atmosphere. Additionally, the correlation analysis
461 under different sea-land conditions indicated that the ground surface is more crucial to the formation of HONO from
462 NO_2 heterogeneous reaction in the inland case, whereas the aerosol surface contributed more in the coastal and sea
463 cases.

464 Furthermore, we found that the HONO/NO_2 in the sea case was about 4.5 times larger than that in the inland case
465 above 600 m when AEC was $\sim 0.2 \text{ km}^{-1}$, and the HONO/NO_2 ratio in the sea case was about 2 times larger than that in
466 the inland case above 600 m when AEC was $\sim 0.8 \text{ km}^{-1}$, which implied that the generation rate of HONO from NO_2
467 heterogeneous reaction in the sea case is larger than that in the inland case in higher atmospheric layers ($> 600 \text{ m}$). To
468 have a deep understanding of three potential contributing factors of HONO production under marine condition, we
469 selected three typical events, which represented the impacts of transport, NO_2 heterogeneous reaction, and unknown
470 HONO source, respectively.

471

472 **Acknowledgements**

473 This research is supported by the National Natural Science Foundation of China (42207113), the Anhui Provincial
474 Natural Science Foundation (2108085QD180), the Presidential Foundation of the Hefei Institutes of Physical Science,
475 Chinese Academy Sciences (YZJJ2021QN06), the National Natural Science Foundation of China (41941011,
476 51778596, 41575021 and 41977184), the Strategic Priority Research Program of the Chinese Academy of Sciences
477 (XDA23020301), the National High-Resolution Earth Observation Project of China (No. 05-Y30B01-9001-19/20-3).
478 We would like to also thank Fudan University (Professor Jianmin Chen's group) for organizing the ship-based
479 campaign and providing meteorological data.

480

481 **Compliance with ethics guidelines**

482 All authors (the name of author) declare that they have no conflict of interest or financial conflicts to disclose.

483

484 **References**

- 485 [1] Alicke B, Geyer A, Hofzumahaus A, Holland F, Konrad S, Patz H W, Schafer J, Stutz J, Volz-Thomas A, Platt U.
486 OH formation by HONO photolysis during the BERLIOZ experiment, *J. Geophys. Res.-Atmos.*, 2003, 108, 8247.
487 [2] Kleffmann J, Gavriloaiei T, Hofzumahaus A, Holland F, Koppmann R, Rupp L, Schlosser E, Siese M, Wahner A.
488 Daytime formation of nitrous acid: A major source of OH radicals in a forest, *Geophys. Res. Lett.*, 2005, 32, L05818.

- 489 [3] Michoud V, Kukui A, Camredon M, Colomb A, Borbon A, Miet K, Aumont B, Beekmann M, Durand-Jolibois R,
490 Perrier S, Zapf P, Siour G, Ait-Helal W, Locoge N, Sauvage S, Afif C, Gros V, Furger M, Ancellet G, Doussin J F.
491 Radical budget analysis in a suburban European site during the MEGAPOLI summer field campaign. *Atmos. Chem.*
492 *Phys.*, 2012, 12, 11951–11974.
- 493 [4] Ryan RG, Rhodes S, Tully M, Wilson S, Jones N, Frieß U, Schofield R. Daytime HONO, NO₂ and aerosol
494 distributions from MAX-DOAS observations in Melbourne. *Atmos. Chem. Phys.*, 2018, 18, 13969–13985.
- 495 [5] Xue C, Zhang C, Ye C, Liu P, Catoire V, Krysztofiak G, Chen H, Ren Y, Zhao X, Wang J, Zhang F, Zhang C,
496 Zhang J, An J, Wang T, Chen J, Kleffmann J, Mellouki A, Mu Y. HONO Budget and Its Role in Nitrate Formation in
497 the Rural North China Plain. *Environ. Sci. Technol.*, 2020, 54, 11048–11057.
- 498 [6] Huang R, Zhang Y, Bozzetti C, Ho K F, Cao J J, Han Y, Daellenbach K R, Slowik J G, Platt S M, Canonaco F,
499 Zotter P, Wolf R, Pieber S M, Bruns E A, Crippa M, Ciarelli G, Piazzalunga A, Schwikowski M, Abbaszade G,
500 Schnelle-Kreis J, Zimmermann R, An Z, Szidat S, Baltensperger U, Haddad I E, Prevot A S H. High secondary
501 aerosol contribution to particulate pollution during haze events in China. *Nature*, 2014, 514, 218–222.
- 502 [7] Zhang B, Wang Y, Hao J. Simulating aerosol-radiation-cloud feedbacks on meteorology and air quality over
503 eastern China under severe haze conditions in winter. *Atmos. Chem. Phys.*, 2015, 15, 2387–2404.
- 504 [8] Wang L, Wen L, Xu C, Chen J, Wang X, Yang L, Wang W, Yang X, Sui X, Yao L, Zhang Q. HONO and its
505 potential source particulate nitrite at an urban site in North China during the cold season. *Sci. Total Environ.*, 2015,
506 538, 93–101.
- 507 [9] Fu X, Wang T, Zhang L, Li Q, Wang Z, Xia M, Yun H, Wang W, Yu C, Yue D, Zhou Y, Zheng J, Han R. The
508 significant contribution of HONO to secondary pollutants during a severe winter pollution event in southern China.
509 *Atmos. Chem. Phys.*, 2019, 19, 1–14.
- 510 [10] Liu J, Liu Z, Ma Z, Yang S, Yao D, Zhao S, Hu B, Tang G, Sun J, Cheng M, Xu Z, Wang Y. Detailed budget
511 analysis of HONO in Beijing, China: Implication on atmosphere oxidation capacity in polluted megacity. *Atmos.*
512 *Environ.*, 2021, 244, 117957.
- 513 [11] Yang Y, Li X, Zu K, Lian C, Chen S, Dong H, Feng M, Liu H, Liu J, Lu K, Li S, Ma X, Song D, Wang W, Yang
514 S, Yang X, Yu X, Zhu Y, Zeng L, Tan Q, Zhang Y. Elucidating the effect of HONO on O₃ pollution by a case study
515 in southwest China. *Sci. Total Environ.*, 2021, 756, 144127.
- 516 [12] Zha Q, Xue L, Wang T, Xu Z, Yeung C, Louie P K K, Luk C W Y. Large conversion rates of NO₂ to HNO₂
517 observed in air masses from the South China Sea: Evidence of strong production at sea surface? *Geophys. Res. Lett.*,
518 2014, 41, 7710–7715.
- 519 [13] Cui L, Li R, Fu H, Li Q, Zhang L, George C, Chen J. Formation features of nitrous acid in the offshore area of
520 the East China Sea. *Sci. Total Environ.*, 2019, 682, 138–150.
- 521 [14] Wen L, Chen T, Zheng P, Wu L, Wang X, Mellouki A, Wang W. Nitrous acid in marine boundary layer over
522 eastern Bohai Sea, China: Characteristics, sources, and implications. *Sci. Total Environ.*, 2019, 670, 282–291.
- 523 [15] Gil G, Kim J, Lee M, Lee G, Lee D, Jung J, An J, Hong J, Cho S, Lee J, Long R. The role of HONO in O₃
524 formation and insight into its formation mechanism during the KORUS-AQ Campaign. *Atmos. Chem. Phys. Discuss.*,
525 2019, <https://doi.org/10.5194/acp-2019-1012>.
- 526 [16] Cui L, Li R, Zhang Y, Meng Y, Fu H, Chen J. An observational study of nitrous acid (HONO) in Shanghai,
527 China: The aerosol impact on HONO formation during the haze episodes. *Sci. Total Environ.*, 2018, 630, 1057–1070.
- 528 [17] Tan W, Liu C, Wang S, Xing C, Su W, Zhang C, Xia C, Liu H, Cai Z, Liu J. Tropospheric NO₂, SO₂, and
529 HCHO over the East China Sea, using ship-based MAX-DOAS observations and comparison with OMI and OMPS
530 satellite data. *Atmos. Chem. Phys.*, 2018, 18, 15387–15402.
- 531 [18] Zhang W, Tong S, Jia C, Wang L, Liu B, Tang G, Ji D, Hu B, Liu Z, Li W, Wang Z, Liu Y, Wang Y, Ge M.
532 Different HONO Sources for Three Layers at the Urban Area of Beijing. *Environ. Sci. Technol.*, 2020, 54,
533 12870–12880.
- 534 [19] Cheng P, Cheng Y, Lu K, Su H, Yang Q, Zou Y, Zhao Y, Dong H, Zeng L, Zhang Y. An online monitoring
535 system for atmospheric nitrous acid (HONO) based on stripping coil and ion chromatography. *J. Environ. Sci.*, 2013,
536 25(5) 895–907.
- 537 [20] Bernard F, Cazaunau M, Grosselin B, Zhou B, Zheng J, Liang P, Zhang Y, Ye X, Daele V, Mu Y, Zhang R,
538 Chen J, Mellouki A. Measurements of nitrous acid (HONO) in urban area of Shanghai, China. *Environ. Sci. Pollut.*
539 *Res.*, 2016, 23:5818–5829.
- 540 [21] Jordan N, Osthoff HD. Quantification of nitrous acid (HONO) and nitrogen dioxide (NO₂) in ambient air by
541 broadband cavity-enhanced absorption spectroscopy (IBBCEAS) between 361 and 388 nm. *Atmos. Meas. Tech.*,
542 2020, 13, 273–285.
- 543 [22] Guo Y, Wang S, Gao S, Zhang R, Zhu J, Zhou B. Influence of ship direct emission on HONO sources in channel
544 environment. *Environ.*, 2020, 242, 117819.
- 545 [23] Meng F, Qin M, Tang K, Duan J., Fang W., Liang S., Ye K., Xie P., Sun Y., Xie C., Ye C., Fu P., Liu J., Liu W.
546 High-resolution vertical distribution and sources of HONO and NO₂ in the nocturnal boundary layer in urban Beijing,
547 China. *Atmos. Chem. Phys.*, 2020, 20, 5071–5092.
- 548 [24] Garcia-Nieto D, Benavent N, Saiz-Lopez A. Measurements of atmospheric HONO vertical distribution and
549 temporal evolution in Madrid (Spain) using the MAX-DOAS technique. *Sci. Total Environ.*, 2018, 643, 957–966.

- 550 [25] Wang Y, Dörner S, Donner S, Bohnke S, Smedt I D, Dickerson R R, Dong Z, He H, Li Z, Li Z, Li D, Liu D, Ren
551 X, Theys N, Wang Y, Wang Y, Wang Z, Xu H, Xu J, Wagner T. Vertical profiles of NO₂, SO₂, HONO, HCHO,
552 CHOCHO and aerosols derived from MAX-DOAS measurements at a rural site in the central western North China
553 Plain and their relation to emission sources and effects of regional transport. *Atmos. Chem. Phys.*, 2019, 19,
554 5417–5449.
- 555 [26] Xing C, Liu C, Wang S, Chan K L, Gao Y, Huang X, Su W, Zhang C, Dong Y, Fan G, Zhang T, Chen Z, Hu Q,
556 Su H, Xie Z, Liu J. Observations of the vertical distributions of summertime atmospheric pollutants and the
557 corresponding ozone production in Shanghai, China. *Atmos. Chem. Phys.* 2017, 17, 14275–14289.
- 558 [27] Xing C, Li C, Wang S, Hu Q, Liu H, Tan W, Zhang W, Li B, Liu J. A new method to determine the aerosol
559 optical properties from multiple-wavelength O₄ absorptions by MAX-DOAS observation. *Atmos. Meas. Tech.*, 2019,
560 12, 3289–3302.
- 561 [28] Xing C, Liu C, Hu Q, Fu Q, Lin H, Wang S, Su W, Wang W, Javed Z, Liu J. Identifying the wintertime sources
562 of volatile organic compounds (VOCs) from MAX-DOAS measured formaldehyde and glyoxal in Chongqing,
563 southwest China. *Sci. Total Environ.*, 2020, 715, 136258.
- 564 [29] Vandaele AC, Hermans C, Simon PC, Carleer M, Colin R, Fally S, Merienne M F, Jenouvrier A, Coquart B.
565 Measurements of the NO₂ absorption cross-section from 42,000 cm⁻¹ to 10,000 cm⁻¹ (238–1000 nm) at 220K and
566 294 K. *J. Quant. Spectrosc. Ra.*, 1998, 59, 171–184.
- 567 [30] Serdyuchenko A, Gorshelev V, Weber M, Chehade W, Burrows J P. High spectral resolution ozone absorption
568 cross-sections –part 2: temperature dependence. *Atmos. Meas. Tech.*, 2014, 7, 625–636.
- 569 [31] Thalman R, Volkamer R. Temperature dependent absorption cross-sections of O₂–O₂ collision pairs between
570 340 and 630 nm and at atmospherically relevant pressure. *Phys. Chem. Chem. Phys.*, 2013, 15, 15371–15381.
- 571 [32] Meller R, Moortgat GK. Temperature dependence of the absorption cross sections of formaldehyde between 223
572 and 323 K in the wavelength range 225–375 nm. *J. Geophys. Res.*, 2000, 105, 7089–7101.
- 573 [33] Rothman L, Gordon I, Barber R, Dothe H, Gamache R R, Goldman A, Perevalov, Tashkun S A, Tennyson J.
574 HITEMP, the high-temperature molecular spectroscopic database. *J. Quant. Spectrosc. Ra.*, 2010, 111, 2139–2150.
- 575 [34] Fleischmann OC, Hartmann M, Burrows JP, Orphal J. New ultraviolet absorption cross-sections of BrO at
576 atmospheric temperatures measured by time-windowing Fourier transform spectroscopy. *J. Photoch. Photobio.*, 2004,
577 A 168, 117–132.
- 578 [35] Stutz J, Kim ES, Platt U, Bruno P, Perrino C, Febo A. UV–visible absorption cross sections of nitrous acid. *J.*
579 *Geophys. Res.-Atmos.*, 2000, 105, 14585–14592.
- 580 [36] Aliwell S, Van Roozendaal M, Johnston P, Richter A, Wagner T, Arlander D W, Burrows J P, Fish D J, Jones R
581 L, Tornkvist K K, Lambert J C, Pfeilsticker K, Pundt I. Analysis for BrO in zenith-sky spectra: an Intercomparison
582 exercise for analysis improvement. *J. Geophys. Res.*, 2002, 107, 4199.
- 583 [37] Liu C, Xing C, Hu Q, Li Q, Liu H, Hong Q, Tan W, Ji X, Lin H, Lu C, Lin J, Liu H, Wei S, Chen J, Yang K,
584 Wang S, Liu T, Chen Y. Ground-based hyperspectral stereoscopic remote sensing network: A promising strategy to
585 learn coordinated control of O₃ and PM_{2.5} over China. *Engineering*, 2021.
- 586 [38] Liu Y, Nie W, Xu Z, Wang T, Wang R, Li Y, Wang L, Chi X, Ding A. Semi-quantitative understanding of
587 source contribution to nitrous acid (HONO) based on 1 year of continuous observation at the SORPES station in
588 eastern China. *Atmos. Chem. Phys.*, 2019, 19, 13289–13308.
- 589 [39] Sun L, Chen T, Jiang Y, Zhou Y, Sheng L, Lin J, Li J, Dong C, Wang C, Wang X, Zhang Q, Wang W, Xue L.
590 Ship emission of nitrous acid (HONO) and its impacts on the marine atmospheric oxidation chemistry. *Sci. Total*
591 *Environ.*, 2020, 735, 139355.
- 592 [40] Huang R, Yang L, Cao J, Wang Q, Tie X, Ho K F, Shen Z, Zhang R, Li G, Zhu C, Zhang N, Dai W, Zhou J, Liu
593 S, Chen Y, Chen J, O’Dowd C D. Concentration and sources of atmospheric nitrous acid (HONO) at an urban site in
594 Western China. *Sci. Total Environ.*, 2017, 593–594, 165–172.
- 595 [41] Xu Z, Wang T, Wu J, Xue L, Chan J, Zha Q, Zhou S, Louie P K K, Luk C W Y. Nitrous acid (HONO) in a
596 polluted subtropical atmosphere: Seasonal variability, direct vehicle emissions and heterogeneous production at
597 ground surface, *Atmos. Environ.*, 2015, 106, 100–109.
- 598 [42] Xing C, Liu C, Hu Q, Fu Q, Wang S, Lin H, Zhu Y, Wang S, Wang W, Javed Z, Ji X, Liu J. Vertical
599 distributions of wintertime atmospheric nitrogenous compounds and the corresponding OH radicals production in
600 Leshan, southwest China. *J. Environ. Sci.*, 2021, 105, 44–55.
- 601 [43] Song Y, Xing C, Liu C, Lin J, Wu H, Liu T, Lin H, Zhang C, Tan W, Ji X, Liu H, Li Q. Evaluation of transport
602 processes over North China Plain and Yangtze River Delta using MAX-DOAS observations.
603 10.5194/egusphere-2022-653.
- 604 [44] Kleffmann J, Kurtenbach R, Lorzer J, Wiesen P, Kalthoff N, Vogel B, Vogel H. Measured and simulated vertical
605 profiles of nitrous acid-Part I: Field measurements, *Atmos. Environ.*, 2003, 37, 2949-2955.
- 606 [45] Stemmler K, Ammann M, Donders C, Kleffmann J, George C. Photosensitized reduction of nitrogen dioxide on
607 humic acid as a source of nitrous acid, *nature*, 2006, 440, 195-198.
- 608 [46] Indarto A. Heterogeneous reactions of HONO formation from NO₂ and HNO₃: a review, 2012, 38, 1029-1041.
- 609 [47] Wang Y, Apituley A, Bais A, Beirle S, Benavent N, Borovski A, Bruchkouski H, Chan K L, Donner S,
610 Drosoglou T, Finkenzeller H, Friedrich M M, Frieß U, Garcia-Nieto D, Gómez-Martín L, Hendrick F, Hilboll A, Jin

611 J, Johnston P, Koenig T K, Kreher K, Kumar V, Kyuberis A, Lampel J, Liu C, Liu H, Ma J, Polyansky O L,
612 Postlyakov O, Querel R, Saiz-Lopez A, Schmitt S, Tian X, Tirpitz J-L, Roozendael M V, Volkamer R, Wang Z, Xie
613 P, Xing C, Xu J, Yela M, Zhang C, Wagner T. Inter-comparison of MAX-DOAS measurements of tropospheric
614 HONO slant column densities and vertical profiles during the CINDI-2 campaign, *Atmos. Meas. Tech.*, 2020, 13,
615 5087-5116.

616 [48] Xu S, Wang S, Xia M, Lin H, Xing C, Ji X, Su W, Tan W, Liu C, Hu Q. Observations by ground-based
617 MAX-DOAS of the vertical characters of winter pollution and the influencing factors of HONO generation in
618 Shanghai, China, *Remote Sens.*, 2021, 13(17), 3518.

619 [49] He S, Wang S, Zhang S, Zhu J, Sun Z, Xue R, Zhou B. Vertical distributions of atmospheric HONO and the
620 corresponding OH radical production by photolysis at the suburb area of Shanghai, China, *Sci. Total Environ.*, 2023,
621 858, 159703.

622 [50] Zhang N, Zhou X, Shepson P B, Gao H, Alaghmand M, Stirm B. Aircraft measurement of HONO vertical
623 profiles over a forested region, *Geophys. Res. Lett.*, 2009, 36(15), L15820.

624 [51] Wong K W, Tsai C, Lefer B, Haman C, Grossberg N, Brune W H, Ren X, Luke W, Stutz J. Daytime HONO
625 vertical gradients during SHARP 2009 in Houston, TX, *Atmos. Chem. Phys.*, 2012, 12, 635-652.

626 [52] Salgado, M. S. and Rossi, M. J.: Flame soot generated under controlled combustion conditions: Heterogeneous
627 reaction of NO₂ on hexane soot, *International Journal of Chemical Kinetics*, 34, 620-631, 10.1002/kin.10091, 2002.

628 [53] Zhou, X., Zhang, N., TerAvest, M., Tang, D., Hou, J., Bertman, S., Alaghmand, M., Shepson, P. B., Carroll, M.
629 A., Griffith, S., Dusanter, S., and Stevens, P. S.: Nitric acid photolysis on forest canopy surface as a source for
630 tropospheric nitrous acid, *Nature Geoscience*, 4, 440-443, 10.1038/ngeo1164, 2011.

631 [54] Kraus, A., Hofzumahaus, A. Field Measurements of Atmospheric Photolysis Frequencies for O₃, NO₂, HCHO,
632 CH₃CHO, H₂O₂, and HONO by UV Spectroradiometry. In: Rudolph, J., Koppmann, R. (eds) *Atmospheric
633 Measurements during POPCORN — Characterisation of the Photochemistry over a Rural Area*. Springer, Dordrecht.
634 https://doi.org/10.1007/978-94-017-0813-5_8.

635 [55] Liu, Y., Nie, W., Xu, Z., Wang, T., Wang, R., Li, Y., Wang, L., Chi, X., and Ding, A.: Contributions of different
636 sources to nitrous acid (HONO) at the SORPES station in eastern China: results from one-year continuous
637 observation. , *Atmospheric Chemistry and Physics Discussions*, 10.5194/acp-2019-219, 2019.

638 [56] Rodgers, C. D., Taylor, F. W. (Ed.): *Inverse methods for atmospheric sounding, theory and practice*, World
639 Scientific, 255 pp.2004.

640 [57] Stutz, J., Kim, E. S., Platt, U., Bruno, P., Perrino, C., and Febo, A.: UV-visible absorption cross sections of
641 nitrous acid, *Journal of Geophysical Research: Atmospheres*, 105, 14585-14592, 10.1029/2000jd900003, 2000.

642 [58] Wang, Y., Apituley, A., Bais, A., Beirle, S., Benavent, N., Borovski, A., Bruchkouski, I., Chan, K. L., Donner, S.,
643 Drosoglou, T., Finkenzeller, H., Friedrich, M. M., Frieß U., Garcia-Nieto, D., Gómez-Martín, L., Hendrick, F.,
644 Hilboll, A., Jin, J., Johnston, P., Koenig, T. K., Kreher, K., Kumar, V., Kyuberis, A., Lampel, J., Liu, C., Liu, H., Ma,
645 J., Polyansky, O. L., Postlyakov, O., Querel, R., Saiz-Lopez, A., Schmitt, S., Tian, X., Tirpitz, J.-L., Van Roozendael,
646 M., Volkamer, R., Wang, Z., Xie, P., Xing, C., Xu, J., Yela, M., Zhang, C., and Wagner, T.: Inter-comparison of
647 MAX-DOAS measurements of tropospheric HONO slant column densities and vertical profiles during the CINDI-2
648 campaign, *Atmospheric Measurement Techniques*, 13, 5087-5116, 10.5194/amt-13-5087-2020, 2020.

649 [59] Wang, Y., Lampel, J., Xie, P., Beirle, S., Li, A., Wu, D., and Wagner, T.: Ground-based MAX-DOAS
650 observations of tropospheric aerosols, NO₂, SO₂ and HCHO in Wuxi, China, from 2011 to 2014, *Atmospheric
651 Chemistry and Physics*, 17, 2189-2215, 10.5194/acp-17-2189-2017, 2017.

652
653

654 **Table 1. Detailed information of the measurement cruise**

Cruise NO.	Periods	Measurement cruise
NO. 1	08:50 to 21:02 19 Apr.	Daishan port (30.24°N, 122.16°E) to Chongming (31.18°N, 121.82°E)
NO. 2	05:40 to 17:45 20 Apr.	Sailing around Chongming island
NO. 3	06:03 21 Apr. to 08:07 03 May	Chongming (31.18°N, 121.82°E) to Zhanjiang port (21.12°N, 110.67°E)
NO. 4	08:07 03 May to 06:52 09 May	Zhanjiang port (21.12°N, 110.67°E) to Daishan port (30.24°N, 122.16°E)
NO. 5	05:40 11 May to 05:55 14 May	Daishan port (30.24°N, 122.16°E) to Qingdao (35.89°N, 120.87°E)
NO. 6	05:55 14 May to 10:00 16 May	Qingdao (35.89°N, 120.87°E) to Daishan port (30.24°N, 122.16°E)

655
656 **Table 2. Detailed retrieval settings of O₄, NO₂, and HONO.**

Parameter	Data source	Fitting internals (nm)		
		O ₄	NO ₂	HONO
Wavelength range		338-370	338-370	335-373
NO ₂	298K, I ₀ -corrected, Vandaele et al. (1998)	✓	✓	✓
NO ₂	220K, I ₀ -corrected, Vandaele et al. (1998)	✓	✓	✓
O ₃	223K, I ₀ -corrected, Serdyuchenko et al. (2014)	✓	✓	✓
O ₃	243K, I ₀ -corrected, Serdyuchenko et al. (2014)	✓	✓	✓
O ₄	293K, Thalman and Volkamer (2013)	✓	✓	✓
HCHO	298K, Meller and Moortgat (2013)	✓	✓	✓
H ₂ O	HITEMP (Rothman et al. 2010)	×	×	✓
BrO	223K, Fleischmann et al. (2004)	✓	✓	✓
HONO	296K, Stutz et al. (2000)	×	×	✓
Ring	Calculated with QDOAS	✓	✓	✓
Polynomial degree		Order 5	Order 5	Order 5
Intensity offset		Constant	Constant	Constant

657
658 * Solar I₀ correction; Aliwell et al. (2002).

659

660

661

Table 3. Error budget estimation (in %) of the retrieved near-surface (0–200 m) trace gas concentrations and AECs, and trace gas VCDs and AOD.

			Error source				Total
			Smoothing and noise errors	Algorithm error	Cross section error	Related to the aerosol retrieval (only for trace gases)	
Cruise route	Near-surface	aerosol	14	4	4	-	15
		NO ₂	16	3	3	15	22
		HONO	20	20	5	15	32
	VCD or AOD	AOD	5	8	4	-	10
		NO ₂	17	11	3	10	23
		HONO	22	20	5	10	32
SUST	Near-surface	aerosol	13	4	4	-	14
		NO ₂	14	3	3	14	20
		HONO	18	20	5	14	31
	VCD or AOD	AOD	5	8	4	-	10
		NO ₂	16	11	3	10	22
		HONO	20	20	5	10	30
CAMs	Near-surface	aerosol	13	4	4	-	14
		NO ₂	15	3	3	14	21
		HONO	19	20	5	14	31
	VCD or AOD	AOD	5	8	4	-	10
		NO ₂	17	11	3	10	23
		HONO	21	20	5	10	31

662

663

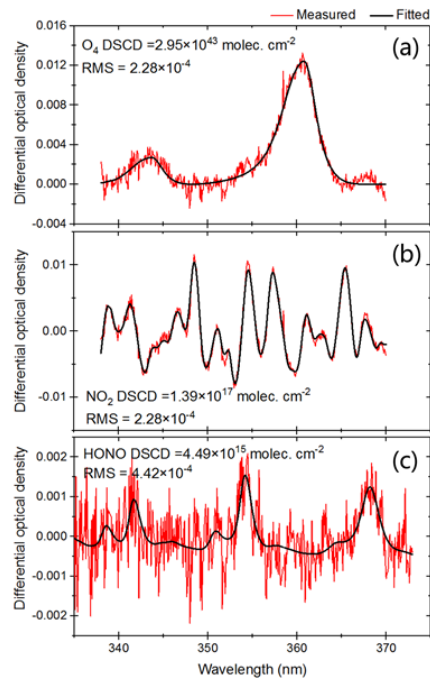


Figure 1. Plots depicting typical DOAS spectral fittings for (a) O₄, (b) NO₂ and (c) HONO.

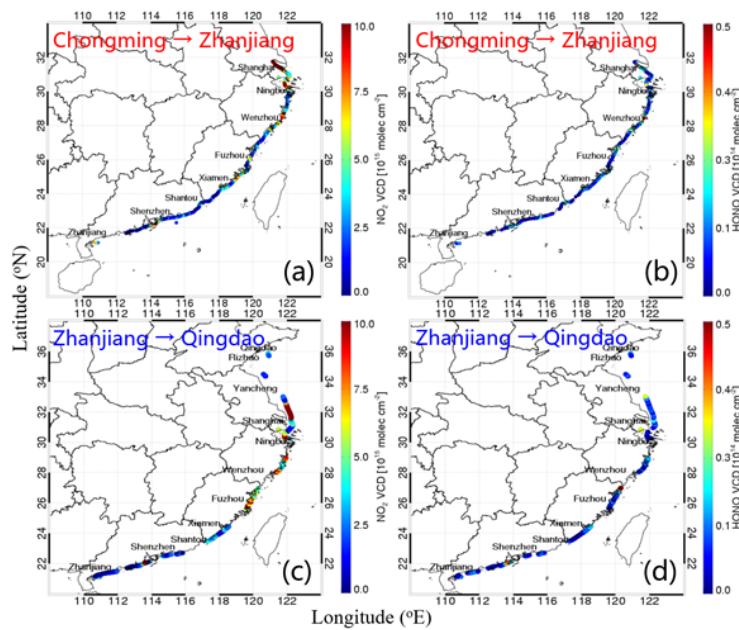
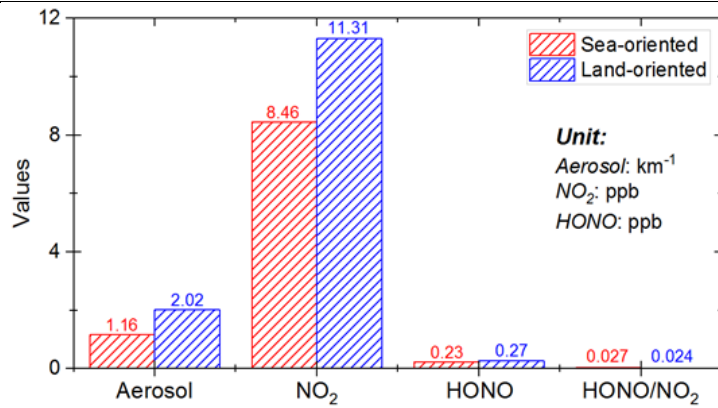
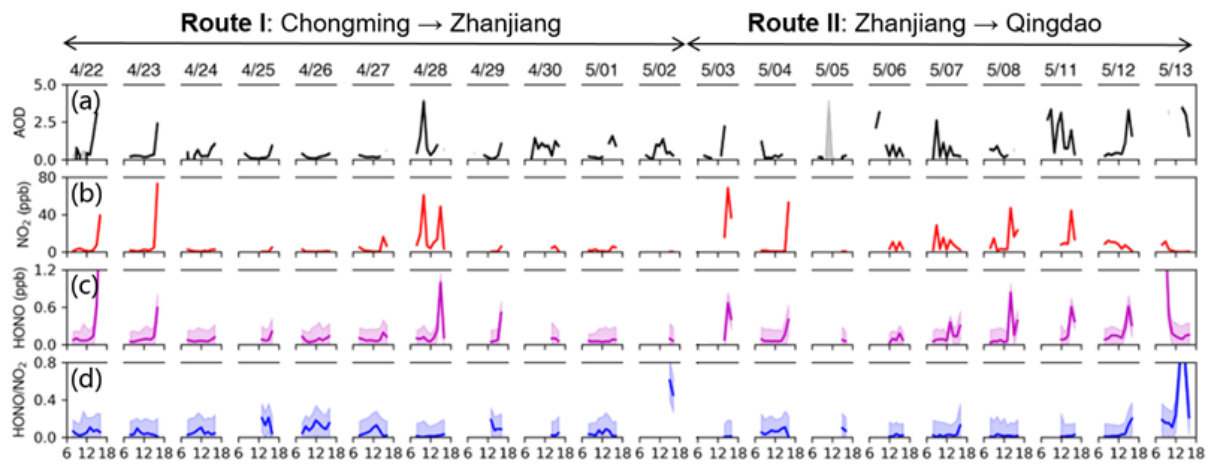


Figure 2. Maps showing the spatial distributions of NO₂ and HONO VCDs. (a) and (b) show the NO₂ and HONO VCDs along the cruise route from Chongming to Zhanjiang. (c) and (d) depict the NO₂ and HONO VCDs along the cruise route from Zhanjiang to Qingdao.



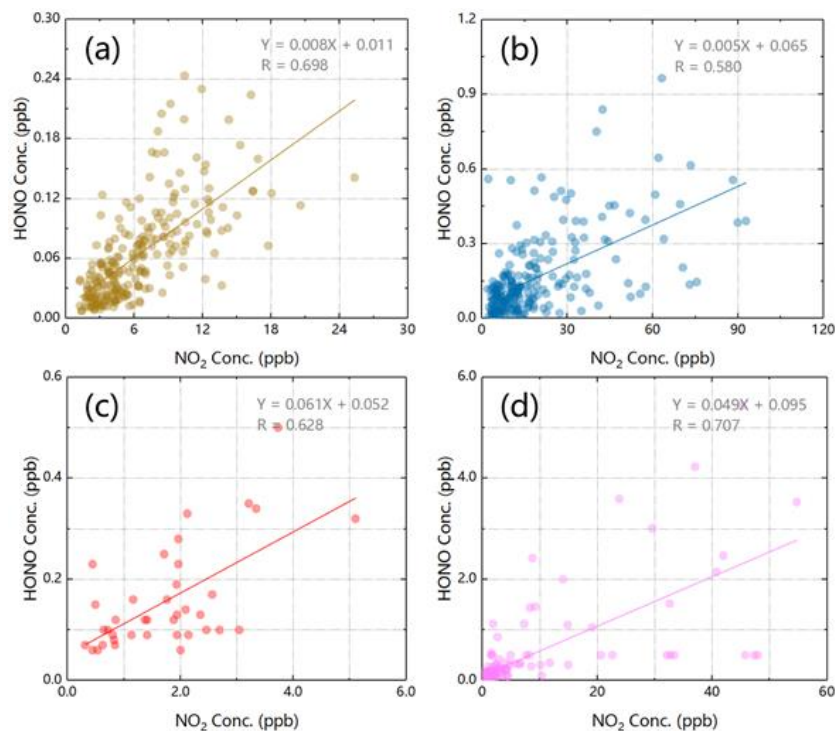
673
674 Figure 3. Bar plots of the averaged aerosol extinction, NO₂ concentration, HONO concentration, and HONO/NO₂
675 ratio during the campaign. The red and blue boxes denote sea-oriented and land-oriented measurements, respectively.

676

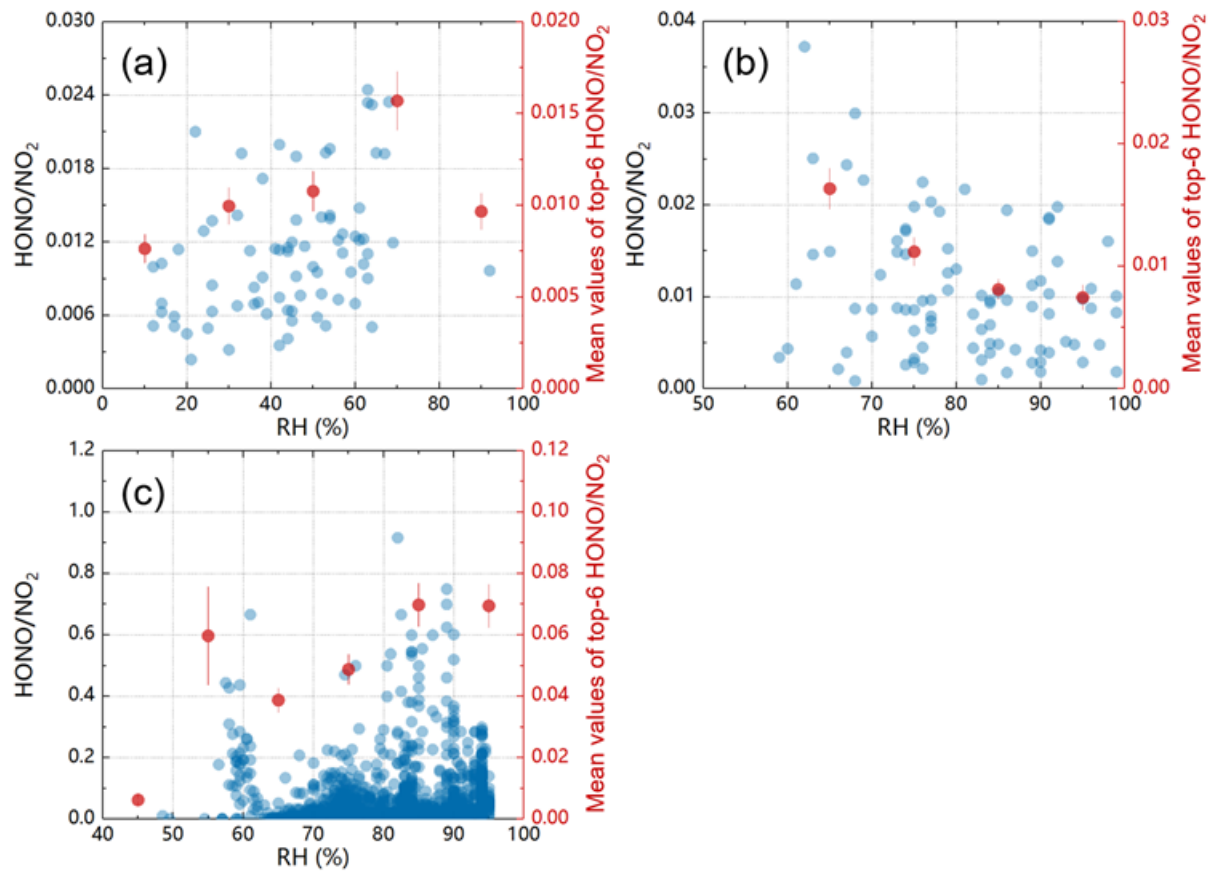


677
678 Figure 4. Histograms of the time series of (a) AOD, (b) surface NO₂ concentration, (c) surface HONO concentration,
679 and (f) surface HONO/NO₂ ratios.

680



681
682 Figure 5. Linear regression plots between surface NO₂ and HONO concentrations in (a) CAMS, (b) SUST, and
683 ship-based measurements of (c) sea-oriented and (d) land-oriented under static weather condition.

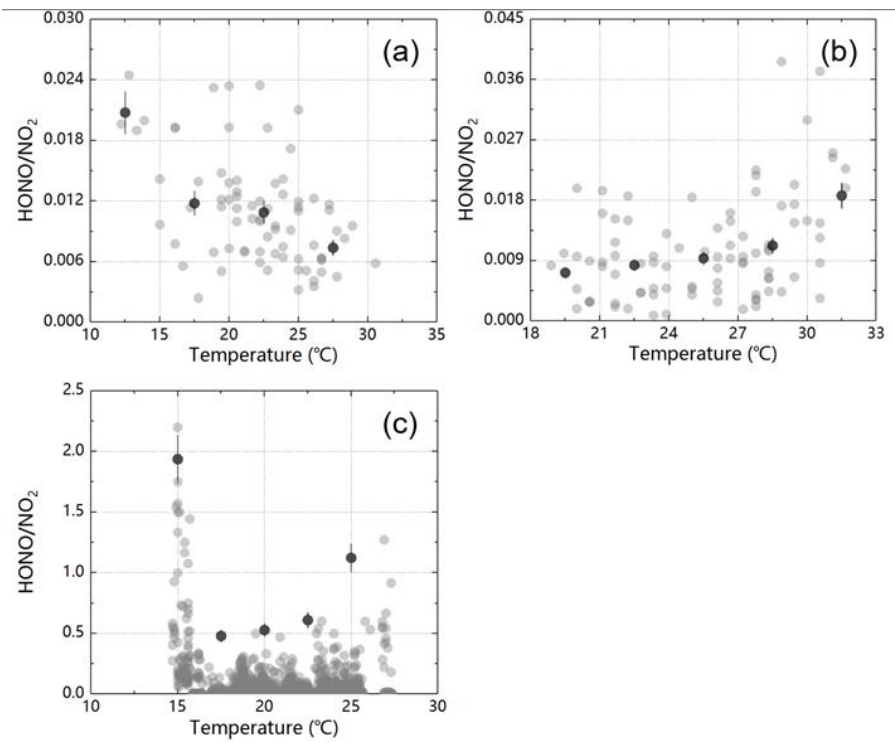


685

686

Figure 6. Scatter plots between RH and HONO/NO₂ ratios in (a) CAMS, (b) SUST, and (c) the ship-based campaign.

687



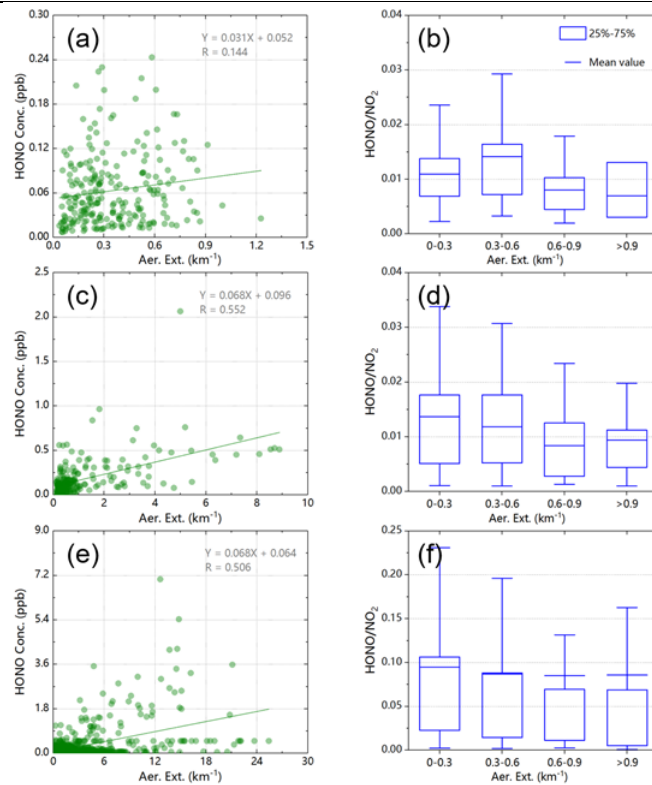
688

689

690

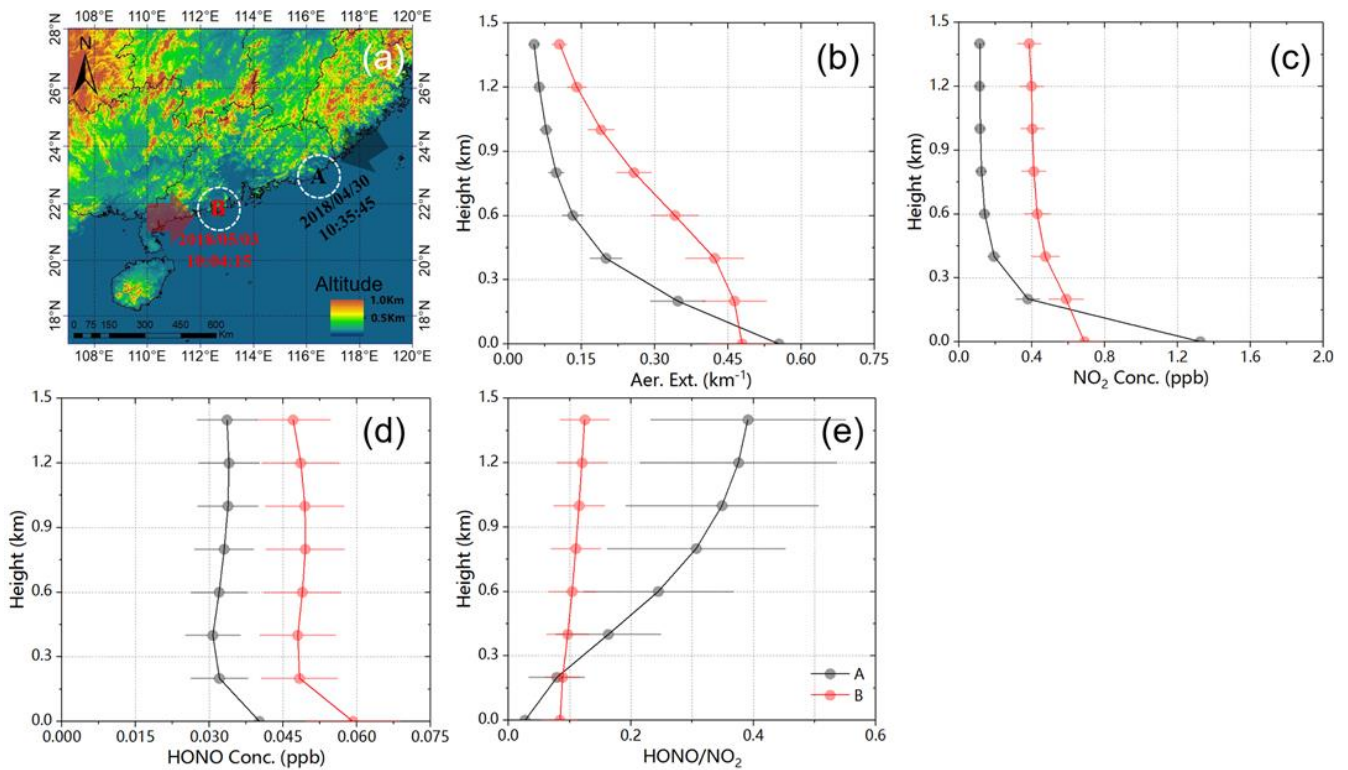
Figure 7. Scatter plots between temperature and HONO/NO₂ ratios in (a) CAMS, (b) SUST, and (c) the ship-based campaign.

691



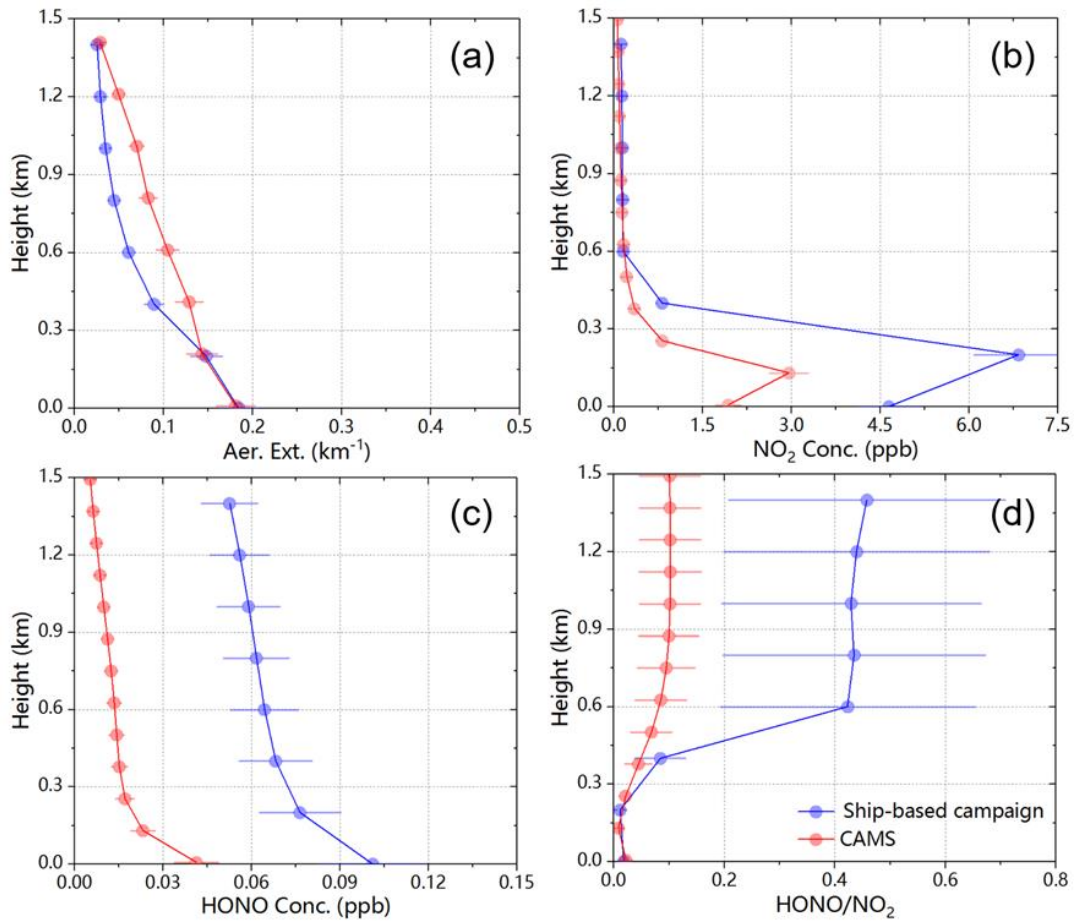
692
 693 Figure 8. (a), (c), and (e) show the linear regression plots between surface aerosol extinction and HONO
 694 concentrations in CAMS, SUST and the ship-based campaign, respectively. Plots (b), (d), and (f) depicts the
 695 HONO/NO₂ ratio distribution under different aerosol extinction coefficient conditions in CAMS, SUST and the
 696 ship-based campaign.

697



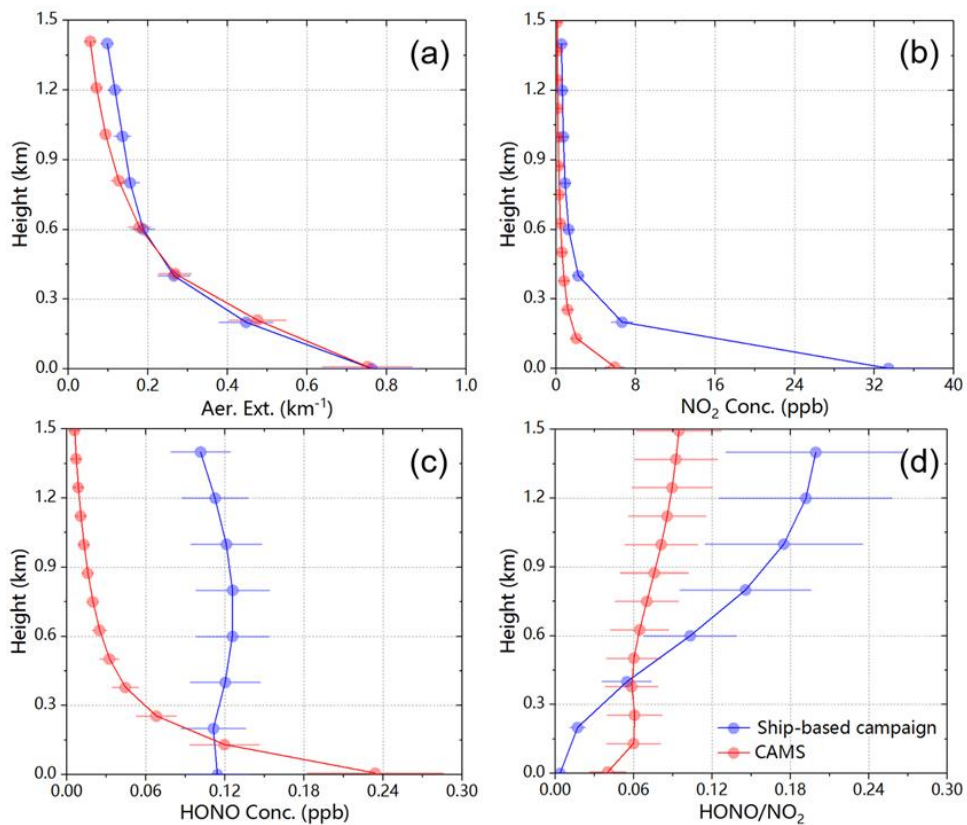
698
 699 Figure 9. Map (a) shows the two measurement points (A: black, sea-oriented with sea wind; B: red, land-oriented with
 700 land wind) during the campaign. Plots (b)–(e) show the vertical profiles of aerosol, NO₂, HONO, and HONO/NO₂
 701 ratios in the above two measurement points, respectively.

702



703
 704 Figure 10. Plots showing the vertical distributions of (a) aerosol extinction, (b) NO_2 concentration, (c) HONO
 705 concentration, and (d) HONO/ NO_2 ratio. The blue and red lines represent a ship-based campaign case and a CAMS
 706 case, respectively.

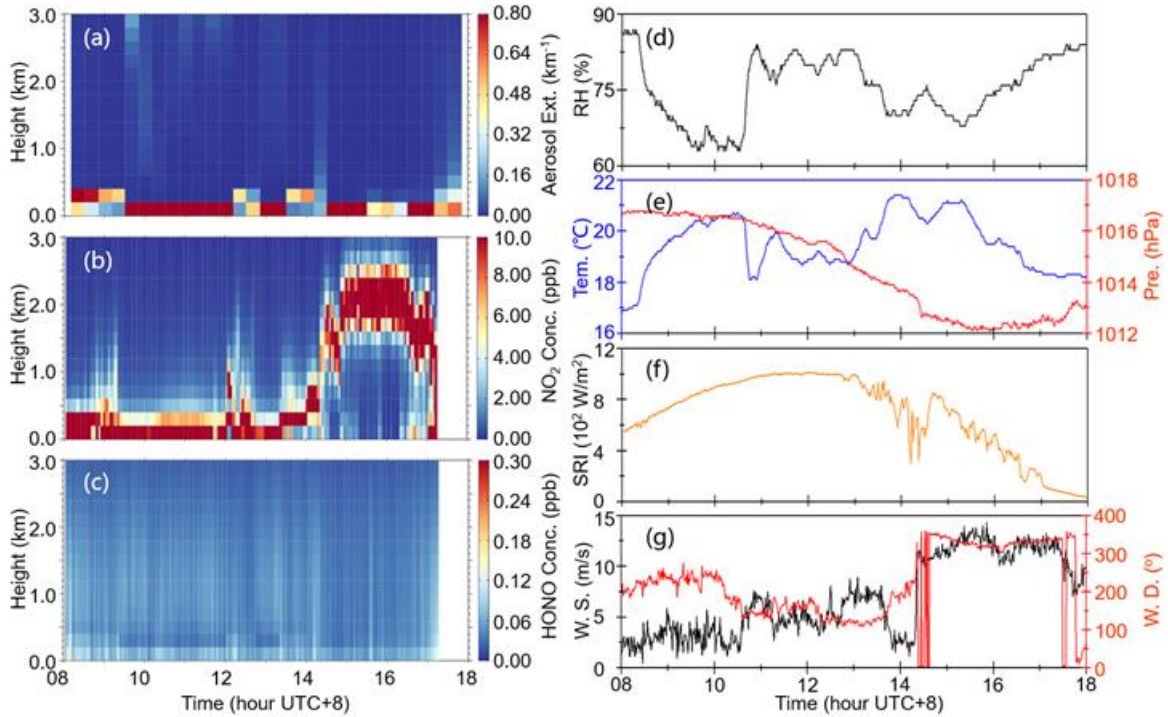
707
 708



709

710 Figure 11. Plots showing the vertical distributions of (a) aerosol extinction, (b) NO₂ concentration, (c) HONO
 711 concentration, and (d) HONO/NO₂ ratio. The blue and red lines represent a ship-based campaign case and a CAMS
 712 case, respectively.

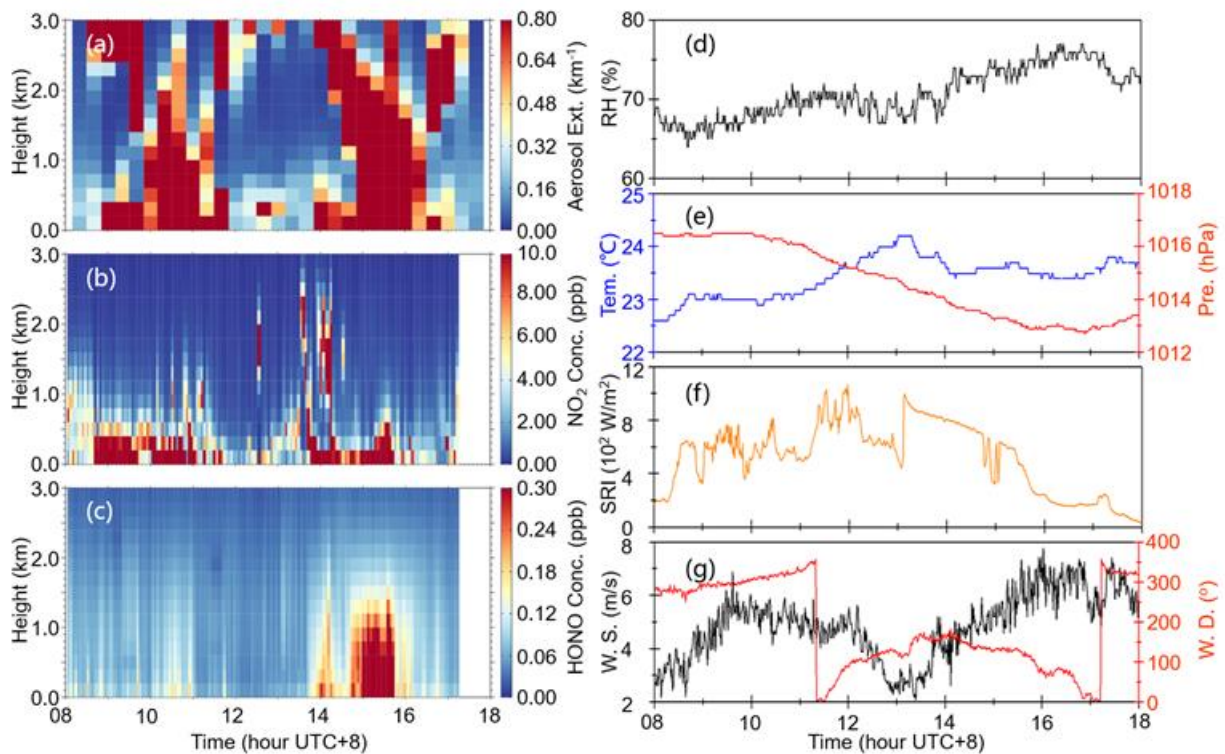
713



714 Figure 12. Case of 20 April 2018. Gradient image showing the time series of (a) aerosol extinction, (b) NO₂, and (c)
 715 HONO vertical profiles. Plot (d) shows the time series of surface RH. Plot (e) depicts the time series of surface
 716 temperature and pressure. Plot (f) shows the time series of surface SRI. (g) depicted the time series of surface wind
 717 speed and wind direction.

719

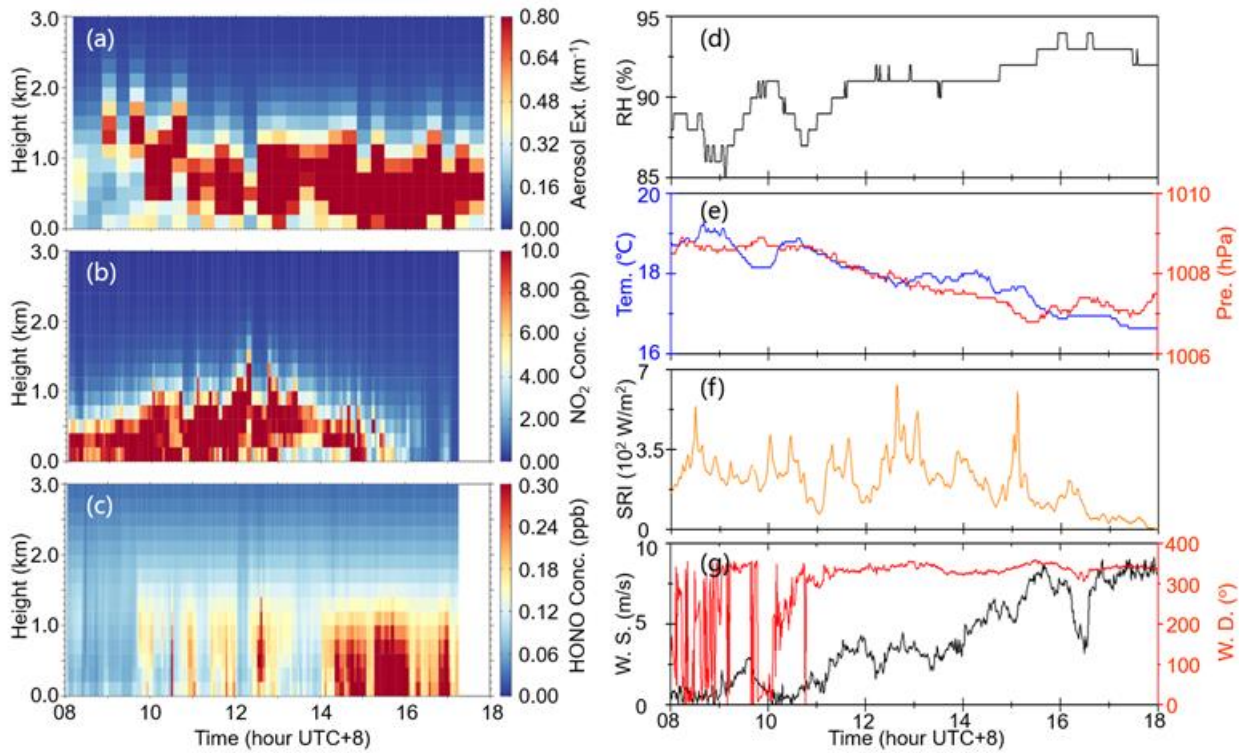
720



721

722
723
724
725
726

Figure 13. Case of 28 April 2018. Gradient image showing the time series of (a) aerosol extinction, (b) NO₂ and (c) HONO vertical profiles, respectively. Plot (d) shows the time series of surface RH. Plot (e) depicts the time series of surface temperature and pressure. Plot (f) shows the time series of surface SRI. Plot (g) depicts the time series of surface wind speed and wind direction.



727
728
729
730
731

Figure 14. Case of 03 May 2018. Gradient image showing the time series of (a) aerosol extinction, (b) NO₂ and (c) HONO vertical profiles, respectively. Plot (d) shows the time series of surface RH. Plot (e) depicts the time series of surface temperature and pressure. Plot (f) shows the time series of surface SRI. Plot (g) depicts the time series of surface wind speed and wind direction.